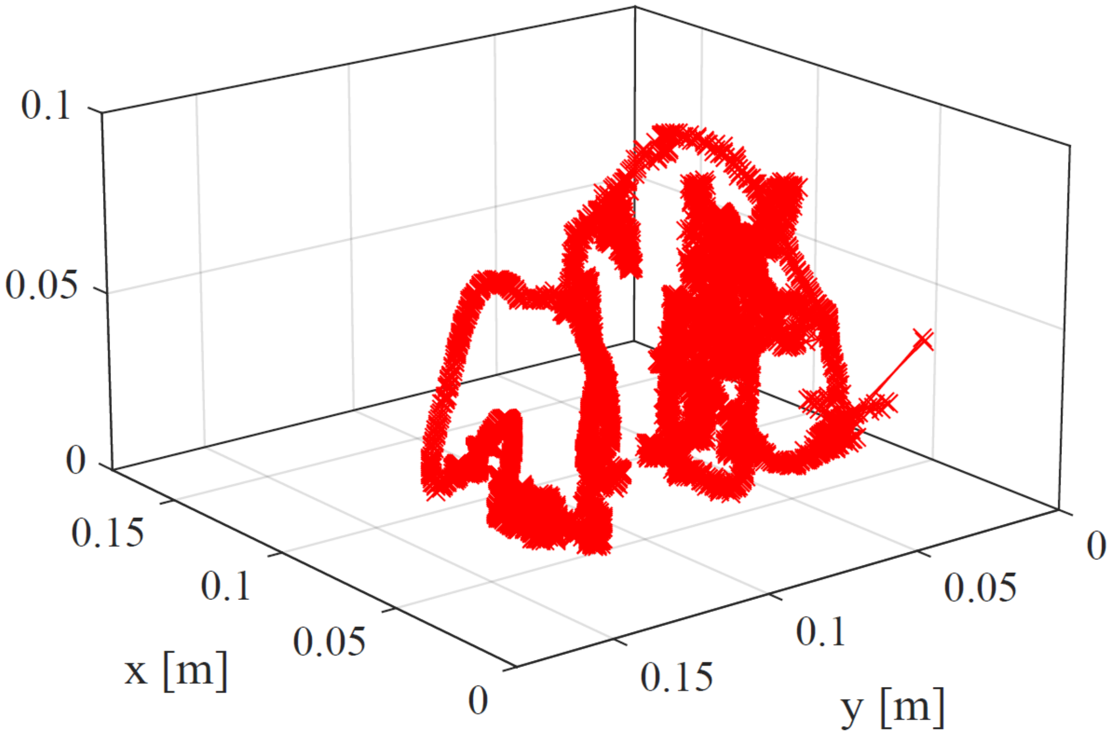

Analysis of fuel mixing in fluidized beds

Measurements with a hot camera probe in the Chalmers gasifier and 3D particle tracking in a cold flow model

Master's Thesis within the Sustainable Energy Systems Programme

ANNA KÖHLER

Department of Energy and Environment
Division of Energy Technology
CHALMERS UNIVERSITY OF TECHNOLOGY
Göteborg, Sweden 2015

MASTER'S THESIS

Analysis of fuel mixing in fluidized beds

Measurements with a hot camera probe in the Chalmers gasifier and 3D particle tracking in a cold flow model

Master's Thesis within the Sustainable Energy Systems programme

ANNA KÖHLER

SUPERVISOR
Erik Sette

EXAMINER
Filip Johnsson

Department of Energy and Environment
Division of Energy Technology
CHALMERS UNIVERSITY OF TECHNOLOGY
Göteborg, Sweden 2015

Analysis of fuel mixing in fluidized beds
Measurements with a hot camera probe in the Chalmers gasifier
and 3D particle tracking in a cold flow model
Master's Thesis within the Sustainable Energy Systems programme
ANNA KÖHLER

© ANNA KÖHLER, 2015

Department of Energy and Environment
Division of Energy Technology
Chalmers University of Technology
SE-41296 Göteborg
Sweden
Telephone: + 46 (0)31-772 1000

Cover: 3-dimensional trajectory of magnetic tracer particle in fluidized bed cold downscaled model.

Chalmers Reproservice
Göteborg, Sweden 2015

Analysis of fuel mixing in fluidized beds
Measurements with a hot camera probe in the Chalmers gasifier
and 3D particle tracking in a cold flow model
Master's Thesis within the Sustainable Energy Systems programme

ANNA KÖHLER
Department of Energy and Environment
Division of Energy Technology
Chalmers University of Technology

Abstract

The present work describes a newly implemented 3D magnetic particle tracking system, which is tested in a fluidized bed down-scaled cold model. The method is used for experimental work with varying fluidization conditions, i.e. different superficial gas velocities, different pressure drops over the air distributor as well as different fixed bed heights. The measurement method obtains the motion of a single fuel particle at any time in the bubbling fluidized bed, which makes it possible to analyse the fuel mixing in fluidized beds. A method to calculate the lateral dispersion coefficient is developed. Further, the measurements of fuel dispersion in a hot industrial gasifier are described and results are compared with the values from the down-scaled model. The values show sufficient agreement.

Analysis proves sufficient robustness of the measurement method and although the experiments are done with a single tracer particle the measurements give statistically expected distribution of many fuel particles moving in a fluidized bed. The presence of mixing cells and flow structures in a bubbling fluidized bed can be visualized in 3 dimensions, while the established bubble flows show expected trends like increasing size of bubble paths with increasing bed height and velocities.

Acknowledgements

This Master thesis is the result of my graduation project at Chalmers University of Technology, Gothenburg Sweden.

I would like to thank my examiner Filip Johnsson for accepting me as a thesis worker for this exciting project, despite his very busy schedule, and his always motivating and helpful feedback. I thank Erik Sette for his professional advice with all matters related to the project, for the detailed introduction to fluidization theory with lively illustrations, for always answering my questions with interesting explanations, for his support in critical situations and his patience – never being tired of clarifying all upcoming ambiguities, and last but not least, for being a wonderful colleague and friend at the division. I would like to thank Ulf Stenman for his help with practical issues in the laboratory and the entertainment in German. I am greatly thankful for my study colleagues and all people I met during my time at the division. Thank you for interesting conversations, delicious fika and your personal as well as academic advice.

Nomenclature

Abbreviations

FBC	Fluidized bed combustion/conversion
FB	Fluidized bed
NO_x	Nitrogen oxides
SO_x	Sulphur oxides
BFB	Bubbling fluidized bed
CFB	Circulating fluidized bed
IEA	International Energy Agency
CO_2	Carbon Dioxide
AMR	Anisotropic Magneto Resistive
CLC	Chemical Looping Combustion
FBG	Fluidized bed gasification
S/R	Set/Reset
PDF	Probability density function
LoG	Laplacian of Gaussian

Greek symbols

ε_{mf}	Void fraction at minimal fluidization
θ	Rotational angle of magnetic sensor
μ	Magnetic moment of permanent magnet
ρ_g	Density of fluidization gas
ρ_s	Density of bed solids
φ	Rotational angle of magnetic sensor

Latin symbols

B	Magnetic dipole
D_x	Lateral dispersion coefficient (x)
f	Sampling frequency
g	Gravitational force
L_{mf}	Bed height at minimal fluidization
p_i	Position measurement i
P_m	Vector of magnetic moment
r_i	Spatial vector of dipole position
t	Time
v	Velocity
Δp_b	Pressure drop over the bed
Δp_d	Pressure drop over the air distributor

Table of Contents

Abstract iii

Acknowledgements v

Nomenclature vii

Table of Contents ix

1 Introduction 1

1.1 Background 1

1.2 Aim and scope 2

2 Theory 3

2.1 Fluidized bed technology 3

2.2 Conversion of solid fuels and applications 3

2.3 Mixing in fluidized beds 5

2.4 Optical measurement methods 6
  2.4.1 Image processing 6
  2.4.2 Particle tracking 7
  2.4.3 Camera calibration 7

2.5 Magnetic particle tracking 8

3 Experimental setup 9

3.1 Measurements under hot conditions 9

3.2 Down-scaled cold flow model 10

4 Methodology 13

4.1 Hot camera probe 13
  4.1.1 Applying image processing 13
  4.1.2 Calculation of the lateral dispersion coefficient 14

4.2 3D particle tracking 15
  4.2.1 Measurement method 15
  4.2.2 Calculations for evaluation 15
  4.2.3 Procedure for particles trapped in corners and bottom region of the bed 16
  4.2.4 Calculation of lateral dispersion coefficient 17

5 Results and discussion 19

5.1 Hot camera probe 19

5.2 Down-scaled cold model 20
- 5.2.1 Robustness of the measurement method 20
- 5.2.2 Influence of the fixed bed height on flow structures 22
- 5.2.3 Influence of the inlet gas velocity on flow structures 24
- 5.2.4 Influence of other factors 25
- 5.2.5 Lateral dispersion coefficient 25

5.3 Comparison of both methods 27

6 Conclusion and suggestions for future work 29

7 References 31

8 List of Figures 32

9 List of Tables 33

1 Introduction

1.1 Background

In the light of substantial changes in the field of power generation towards decreased greenhouse gas emissions, conventional combustion technologies with coal, oil and gas forfeit their reputation, while energy from renewable sources such as wind and solar power exhibit a strong growth during the last 10 years and are expected to keep on growing (Figure 1.1).

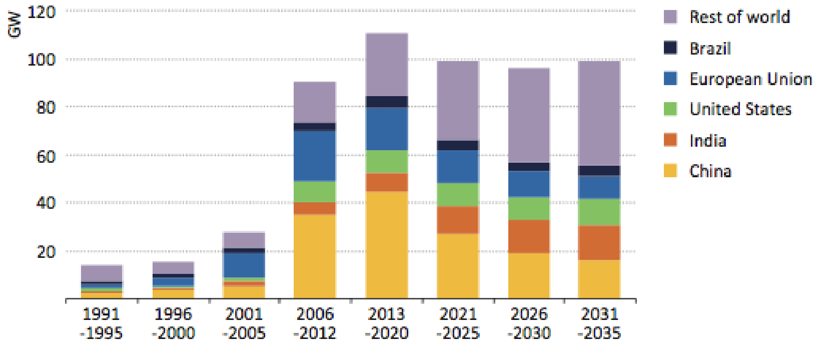

* Excludes capacity that directly replaces retired capacity of the same technology type.

Figure 1.1: Average annual increases in renewables-based capacity* by regions. From the New Policies Scenario of the IEA World Energy Outlook 2013 [1]

Institutions like the International Energy Agency (IEA) predict worldwide an increase in total installed capacity by a factor of 2.5 from 2012 to 2035, where wind, solar and hydro power register the largest additions [1]. However, there are different ways of reducing CO_2 emissions in heat and power production and the world's energy situation demands a versatile solution. High fractions of intermittent sources in power production results in fluctuations in the grid, which makes it difficult to adjust production to the load, i.e. leads to an unbalanced energy system requiring grid extension, control technologies or balancing power, such as thermal power [2].

An example for CO_2-neutral load balancing is the usage of biomass in non-intermittent power production. Further, the replacement or extension of already existing technologies to become carbon neutral, meaning for example fossil fuel powered plants with carbon capture and storage (CCS), is cost-demanding as know-how and installation is not in place yet, where on the other hand fuel-shift to renewable sources such as biomass is often cheaper to implement [3]. However, for thermal power technologies the change of fuel is very likely coupled to a decrease in efficiency as for instance biomass from household and wood waste has a lower heating value and is due to moisture and volatile content more difficult to handle [4].

When converting low-grade fuels fluidized bed (FB) reactors stand out with a number of benefits. The technology was first commercially used in power generation in the 1970s [5] and has since then increased its usage by growing numbers and size of boilers as well as its range of applications, for example in gasification. Despite its miscellaneous usage there is still a lack of detailed understanding of the mixing processes in the fluidized bed [6], which becomes in particular important for the reactor design and plant performance when varying applications [7].

Vertical mixing processes in the fluidized bed is desired to be very high, however, the lateral mixing determine how fast fuel is spread over the bed, where different applications require different speed of fuel spreading. As in combustion and direct gasification fuel is converted relatively fast, transition over the bed should happen accordingly [8], while on the other hand indirect gasification requires a longer residence time of the fuel particles in the reactor [9]. In large combustion applications an increased number of fuel feeding ports can make up for slow spreading fuel particles by shorten the distance the fuel particles have to travel, but is connected to increased investment cost.

A common parameter to describe how fuel is spreading over the bed in horizontal direction is the lateral fuel dispersion coefficient expressed in meters squared per seconds, which is a crucial design parameter for all different applications, when aiming for cost efficient operation of plants. In literature one often makes recourse to experimental approaches to determine the lateral dispersion coefficient and literature data varies over several orders of magnitude [10]. The lateral dispersion coefficient is found to depend on reactor size and design in combination with operational conditions of the bed [11], [12]. The measurements are often conducted at ambient conditions in small beds in disregard of fluid-dynamical scaling laws and their results are therefore seldom transferable to coefficients of industrial sized units operated at elevated temperatures. Experiments are costly and time intensive, where measurements at ambient conditions in simplified geometries seem not to be able to capture complex flow patterns as they occur in fluidized bed boilers. Modelling tools come along with numerous uncertainties and are seldom less time consuming [6], [8].

This work presents two measurement methods in both hot and fluid-dynamically downscaled cold flow conditions. The measurements for hot conditions are run in an industrial-scale fluidized bed 2-4 MW indirect gasifier [13], which is connected to a CFB boiler [14]. The chamber of the gasifier can be accessed by a hot camera probe to capture fuel movement on the surface of the bed. The second measurement method is applied at a fluid-dynamically downscaled bubbling fluidized bed [15] running at ambient conditions as it was developed similar to a work by Sette et al. [16]. The particles' movement can be tracked in all three dimensions and two rotational angles using a novel anisotropic magneto resistive sensor system.

1.2 Aim and scope

The aim of the present project is to plan and conduct the experimental work with the 3D particle tracking system in the cold down-scaled unit and to develop an analysis method for the test results in order to gain quantitative information about the solids mixing mechanisms in fluidized beds. Further, experiments with the hot camera probe in the Chalmers' gasifier and their evaluation are followed to understand the analysis of the lateral fuel dispersion in an industrial-scale unit and be able to compare results with those gained from the cold down-scaled model.

2 Theory

2.1 Fluidized bed technology

The fluidized bed technology in thermal power generation evolved with the goal to have higher fuel flexibility as well as better controllability of emissions inside the combustion process. Both features are still the main advantages the technology has ahead of others according to Koornneef et al. [5].

The technology's name is derived from its granular solid bed, which consists of sand and recirculated ash from the combustion process in varying composition depending on the ash content of the used fuel. Further additives such as limestone for desulfurization, catalytic materials among others for tar reduction or oxygen carriers in chemical looping combustion (CLC) applications can be added to the bed. The bottom of dense fluidized bed is equipped with a so-called air distributor making it possible to pass gases through the solids and suspend them. Depending on the application and size there are various distributor designs, such as perforated plates (used in the cold model of the present work), plates spiked with nozzles (common in industrial scale beds) or tubes with mounted nozzles. At so-called minimum fluidization velocity, where drag force balances the gravity, the particles become fluidized, meaning the solid bed turns into a formation which behaves like a bubbling liquid of low viscosity [17].

Finally, fuel is fed into the reactor, where the fluidized bed promotes a rapid dispersion, high levels of contact between the gases and solids as well as a good thermal transport, thus fosters efficient combustion and a high heat transfer between the bed and the water tube walls of the reactor. The high thermal inertia of the sand keeps the bed at an even temperature and allows the conversion of low-grade fuels with low heating value and high ash, water or volatile content. This makes the process applicable for a variety of fuels such as municipal waste, coal, sludge and wood waste without the need of expensive fuel-preparation.

The emission of nitrogen oxides (NO_x) is usually lower compared to other conventional technologies as the temperature can be kept constant below numbers, which are crucial for NO_x formation. Typical values in fluidized bed boilers are given by Koornneef et al. [5] to be around 760-900 °C, while thermal NO_x is formed at temperatures above 1500 °C. Sulphur emissions (SO_x) can be controlled directly in the boiler by adding limestone, which in a number of reactions converts SO_2 into gypsum. This product can among other non-hazardous by-products be re-used (for example in building construction).

There are two variants of the technology used in FBC and FBG applications: bubbling fluidized beds (BFB) and circulating fluidized beds (CFB), where the latter has an additional external loop to recirculate bed material back into the process. Several mentioned features make FB also attractive for gasification applications, where instead of heat and power syngas for further usage is produced.

2.2 Conversion of solid fuels and applications

Any solid fuel conversion, i.e. combustion or gasification, is divided into three steps: drying, devolatilisation, respectively pyrolysis, and char conversion. While combustion is an exothermic reaction with oxygen, gasification reactions are slower and endothermic. Drying and devolatilisation are driven by heat, while the char part of the fuel also needs a reactant to convert, which is in the case of gasification e.g. water vapour, oxygen or carbon dioxide reacting to carbon monoxide and hydrogen. Other products such as methane, hydrocarbons and tars lower the quality of the raw gas.

In FB applications for (direct) gasification both reactor types (BFB and CFB) are common [18]. Here the fuel is partly combusted within the reactor to keep a sufficient temperature. The remaining part is then directly gasified with reactants varying from steam to pure oxygen or air, where the latter is cheapest, but causing a high dilution of the raw gas with nitrogen (Figure 2.1).

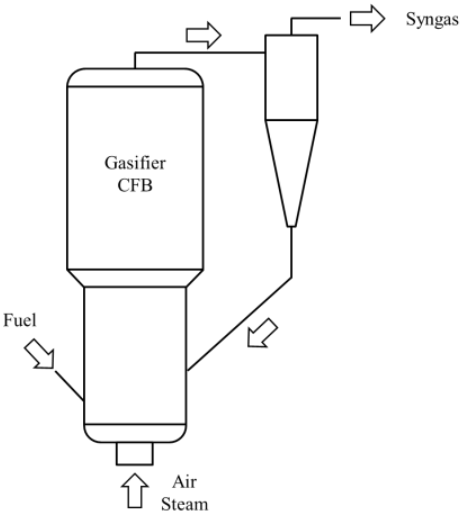

Figure 2.1: Schematic of gasifier

A fairly new type of the technology is the dual fluidized bed (DFB) for indirect gasification [19]. In this case raw gas dilution from flue gas or air can be avoided by using two separate but interconnected reactors (Figure 2.2). On the one side a FB combustor fed with fuel and air provides the heat, which is required for the gasifier on the other side. The heat for the gasifier is transported by the circulating bed material. Additionally steam is fed into the bottom of the gasifier for fluidization of the bed and provision of reactants. The loop between the reactors is closed by two steam fluidized seals, providing heat from one side of the gasifier and returning unconverted char back to the combustor [13].

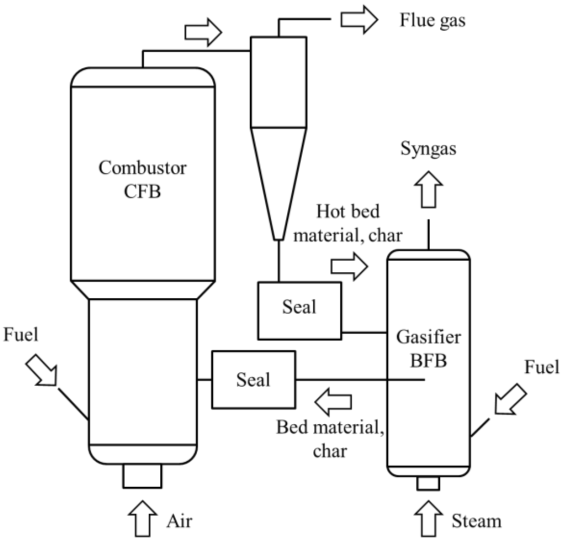

Figure 2.2. Schematic of the Chalmers Dual Fluidized bed combustor and gasifier

The combustor can be used in a conventional way for heat and power production, yet with reduced energy utilisation to meet the gasification’s energy demand, and raw gas production in the gasifier can be adjusted to e.g. market prices or fuel availability. The two main advantages are that heat and reactants are provided without raw gas dilution and the fuel is completely converted either in the gasifier or the combustor.

2.3 Mixing in fluidized beds

Already before the intensive usage of fluidized beds in various industrial applications, Rowe et al. [20] found that bubbles forming at the air inlet of the bed cause displacement patterns, thus forcing the particles to move. Each bubble sets three processes going: While bed material is displaced by the rising bubble, the particles drift downwards around the bubble's surface [21]. On the bottom the bubble pulls up a so-called wake in which particles are mixed and lifted upwards (Figure 2.3a) [22]. The wake drags in and pushes out bed material, while gaps from lifted material are filled with other sinking particles (Figure 2.3c). Finally, when reaching the surface the bubble erupts and scatters material in the bed (Figure 2.3b) [11].

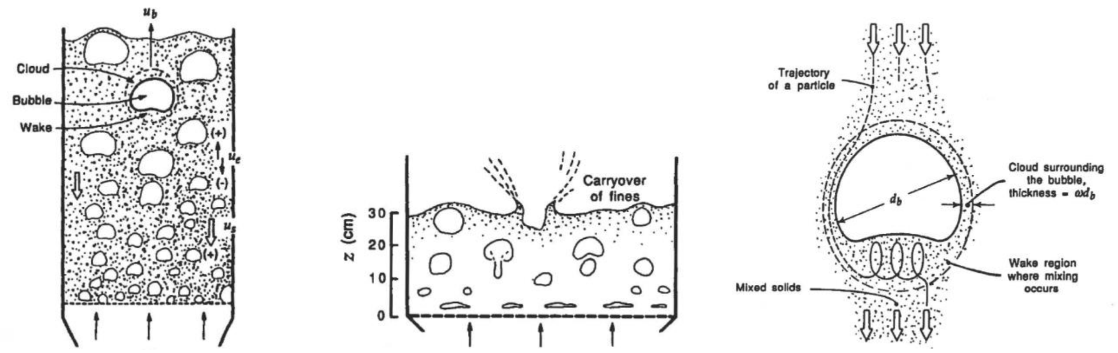

(a) (b) (c)

Figure 2.3: a) Bubbles rising in a fluidized bed with the velocity u_b. b) An erupting bubble on the bed surface results in carryover of particles. c) Schematic of a rising bubble with indication of solids moving around the bubble. [23]

By increasing the mass flow rate of the gas into the bed, bubbles are formed continuously and causing the fluidization of the whole bed. For the fluidized bed the quantity of solid mixing, respectively solid fuel mixing over the bed can be expressed in an overall lateral fuel dispersion coefficient, meaning the three mechanisms are taken together and simplified while assuming isotropic mixing in both lateral directions.

Pallarès et al. [8] found that fuel particles in a 2D fluidized bed move in flow patterns similar to horizontally-aligned vortexes, which are induced by the uprising bubble flow, a so-called bubble path. Each vortex, which can be interpreted as the vertical cross-section of a toroid, forms a separate mixing cell. The particles are dragged up-wards in the centre of the toroid, where rising bubbles are concentrated, and sink back to the bottom bed on its outside (Figure 2.4a).

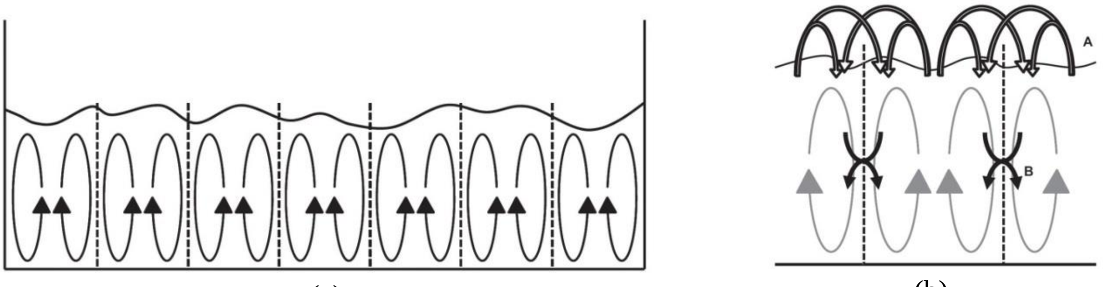

(a) (b)

Figure 2.4: a) Assumed mixing pattern as exemplified by Olsson et al. [24] based on the results from Pallarès et al. [8]. b) Mechanisms contributing to lateral mixing: bubble eruption scattering (A) and drift sinking (B).

All three mechanisms mentioned before are still present in the cells and contribute to fuel mixing in the bed, whereas the influence of emulsion drift sinking and bubble eruption is believed to be most crucial for movement in lateral direction [24]. This is due to the fact that only the movement, resulting in solids changing mixing cells, is considered to add up to the net lateral mixing. Figure 2.4b shows how the drift sinking and the scattering due to bubble eruption can result in particles changing their mixing cell.

So far the described flow structures were confirmed with experimental work in two dimensions [8], and a next step should be to also investigate if the same principal flow structure is present in a 3D system. There are different approaches for indirect and direct measurements of the lateral fuel dispersion coefficient in industrial scale units under hot conditions, among others, the measurement of water concentrations above the bed [25] or the visual examination with the hot camera probe, as done in this work. However, these methods are limited to the bed surface, cannot follow the movement of fuel particles inside the bed and are therefore unsuitable for the observation of flow patterns. A wider range of measurement methods, thus better accessibility to particles inside the dense bed is provided by cold models in laboratory scale and the consideration of fluid-dynamical scaling according to Glickman's scaling laws [15] assure that fluid behaviour and flow patterns are relatively similar to those in industrial-scale devices. The scaling method applied on the fluidized bed used for this work was elaborated and tested by Sette et al. [16].

2.4 Optical measurement methods

As mentioned before, there are a number of methods to follow fuel particles in fluidized beds to be able to analyse their movement and measure for example the lateral dispersion coefficient. Beside the measurements in a down-scaled cold model this work evaluates the measurements done with a hot camera probe. Measurement data is available as videos, i.e. image sequences, which have to be processed to be able to extract information.

2.4.1 Image processing

An image is a number of points (pixels), which are arranged in form of a matrix, where the matrix' values stand for different intensities. Thus for an image with n×m pixels in grayscale a n×m×1 matrix is needed to describe the image, while a coloured image is a n×m×3 matrix. To extract information from an image with an object on certain background, image processing is used as a tool to find unique features of the object and be able to distinguish it from the background with a computer. In the case of the current work the task is to find unique features of the fuel particles on the background of the fluidized bed to be able to detect them and to track them to gain information about their movement.

There are numerous filter functions to smooth images and delete noise to make it possible to distinguish the desired object from the background. A common filter is the Gaussian function with the known bell shape (Figure 2.5a), which removes detail by being convolved over an image. This means the much smaller filter matrix (Figure 2.5b) is laid over the image, for every point in the middle of the filter function a weighted average is calculated with the values of the filter template and by moving the filter further over the image the whole image is smoothed. Depending on the size of the filter function it removes small irregularities on the image, but at the expense of losing features.

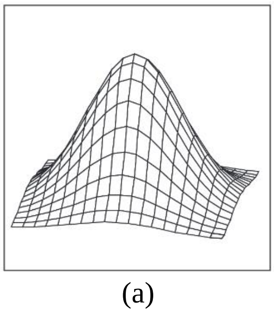

(a)

0.002	0.013	0.022	0.013	0.002
0.013	0.060	0.098	0.060	0.013
0.022	0.098	0.162	0.098	0.022
0.013	0.060	0.098	0.060	0.013
0.002	0.013	0.022	0.013	0.002

(b)

Figure 2.5: Gaussian function [26]. (a) Well-known shape of the Gaussian bell. (b) Example of a template for a 5×5 Gaussian filter function.

Another tool to distinguish objects from their background is the histogram based thresholding. By drawing the histogram of an image's matrix the intensity values for the background and the desired object can be identified and all values outside the range of the object can be set to 0 (Figure 2.6). Now the information for everything but the object is removed, thus the objects remain as so-called blobs on a unified background, which can be detected easily and assigned to an identity (blob detection).

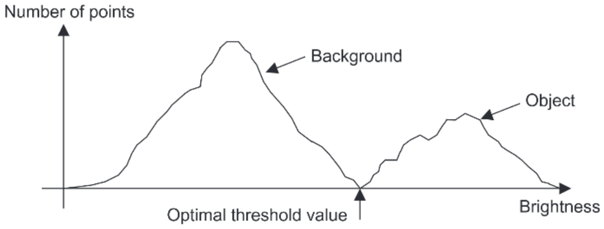

Figure 2.6: Finding optimal value for thresholding [26].

2.4.2 Particle tracking

To track a particle over a sequence of images the object's identity have to be maintained over the subsequent images. However, this can be problematic when tracking multiple particles which might overlap or if the particle disappear from the image for certain frames. To maintain the identities of individual particles Kalman filtering can be used, which predicts the objects' next positions by processing information about the previous detections as well as the velocities of the objects. The predictions can then be assigned to the next detections by minimizing the distances between all predictions and detections (cost function), i.e. every detection gets assigned to the prediction closest to it. If objects are invisible for too many frames they are deleted and newly appearing objects get a new identity. The number of frames after which an object is deleted can be set by a threshold.

2.4.3 Camera calibration

As mentioned before the information about particles position in the image is available in pixels. To be able to translate the information into world coordinates the camera has to be calibrated. Every camera has imperfections as for example a real lens is spherical not parabolic, causing that points far away from the optical centre are bent (Figure 2.7a). It is also practically impossible to align the lens perfectly to the camera's imager, which creates tangential distortions as the effect can be seen in Figure 2.7b [27].

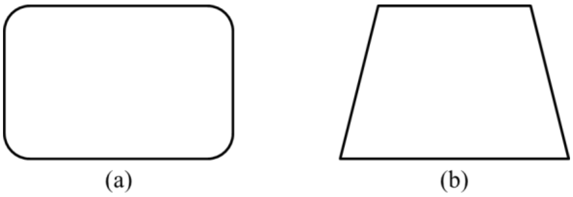

Figure 2.7: Effect of camera imperfections on image. (a) Spherical lens bents points away from the optical centre. (b) Miss-alignment of lens and imager causes tangential distortion.

By taking a number of pictures of a known object (e.g. a checker board) from different viewpoint, i.e. rotations and translations, the relative location and orientation of the object to the camera can be calculated (extrinsic parameters). Further the intrinsic parameters of the camera can be derived from the extrinsic parameters. This procedure is implemented in Matlab using the correction terms explained in more detail in the work by Bradski and Kaehler [27].

To measure objects or positions in images the same checker board can be used and compared to the object to be measured.

2.5 Magnetic particle tracking

The optical methods for tracking objects are limited on the visibility of the objects and can only predict the particles position when they appear on the bed surface. To follow objects inside the dense bed a variety of particle tracking methods as they can be used for laboratory scale setups are discussed by Mohs et al. [28], where non-intrusive magnetic particle tracking has a number of advantages ahead of others. A main benefit of this method is that both position and orientation of the tracer particle can be measured in all 3 dimensions, while it is relatively cheap and does not require exceptional safety precautions.

As the name of the method indicates the tracer is a permanent magnet, which is in the present work tracked by four sets of 3-axis sensors, i.e. a total of 12 measurements are collected at each sampling point. The sensor sets are positioned at each side of the fluidized bed and each set contains three perpendicular sensing elements based on a Permalloy film with a default magnetization direction, i.e. all three Cartesian directions x, y and z are obtained by every sensor set [29]. Permalloy is a nickel-iron alloy known for its high magnetic permeability, which is beneficial for sensing external magnetic fields. They affect the magnetization direction of the Permalloy, which can be measured as change in resistance for an electrical current flowing through the sensing element [30].

The tracking of the permanent magnet is an inverse problem, where its quasi-static magnetic field is modelled as the field of a magnetic dipole with six degrees of freedom: position in x, y and z, rotation in φ and θ and magnetic moment μ. As the magnetic moment μ_0 of the tracer can be obtain beforehand the problem is reduced to five degrees of freedom [31]. The field of a magnetic dipole towards the sensor i ($i=1$ *to* N, *with* $N=3$) can be described as [32]

$$\boldsymbol{B_i} = \frac{\mu_0}{4\pi}\left(-\frac{\boldsymbol{P_m}}{|\boldsymbol{r_i}|^3} + \frac{3(\boldsymbol{P_m}\cdot\boldsymbol{r_i})\boldsymbol{r_i}}{|\boldsymbol{r_i}|^5}\right) \tag{1}$$

Here $\mathbf{P_m}$ is the vector of the magnetic moment defined according to Eq. (2).

$$\boldsymbol{P_m} = p_m[\sin(\theta)\cos(\varphi), \sin(\theta)\sin(\varphi), \cos(\theta)] \tag{2}$$

The vector $\mathbf{r_i}$ is the spatial vector from the dipole position to the position of the sensor i

$$\boldsymbol{r_i} = [(x_i - x_0), (y_i - y_0), (z_i - z_0)] \tag{3}$$

With the used 4×3 sensor elements the problem is over-determined and can be solved with a non-linear optimization algorithm, which minimizes the sum of the squared error between the predicted $\mathbf{B_i^{simulation}}$ and the $\mathbf{B_i^{meas}}$ from the sensors' measurements [31]

$$Q = \sum_{i=1}^{N}\left(B_i^{meas} - B_i^{simulation}\right)^2 \tag{4}$$

As long as the tracer magnet does not come too close to the sensing element, so that the external magnetic field does not get too strong, the sensor is able to return to its default magnetization direction, when the external field departs from the sensor. On the other hand if the tracer magnet comes too close, the sensor saturates and has to be restored. This is done with a coil surrounding the sensor, which is magnetized with two short electrical pulses and so resets the default magnetization. The so-called set/reset (S/R) is associated with a time delay in the measurement, thus can be problematic for high sampling frequencies.

3 Experimental setup

3.1 Measurements under hot conditions

The measurements with the hot camera probe were conducted in the Chalmers 2-4 MW indirect gasifier, where the connected combustor is a 12 MW_{th} CFB boiler fired with wood chips and provides the required heat to the gasifier. After reaching an operating temperature of around 800 °C slightly below atmospheric pressure, the interconnecting loop seals are turned off and the steam mass flow into the gasifier can be adjusted to desired velocities as they are shown in Table 3.1. The gasifier runs now in a kind of bubbling fluidized bed condition with no recirculation of solids through the seals. The used bed material is silica sand with a particle size of 300 µm and the bed height is 0.3 m (Table 3.2). The camera is installed 1 m above the bed surface in an angle of 45 degree (Figure 3.1).

Table 3.1: Measured velocities in Chalmers gasifier (no circulation)

		Test A	Test B	Test C
Steam in	kg/h	95	140	180
Fluidization velocity	m/s	0.089	0.132	0. 182

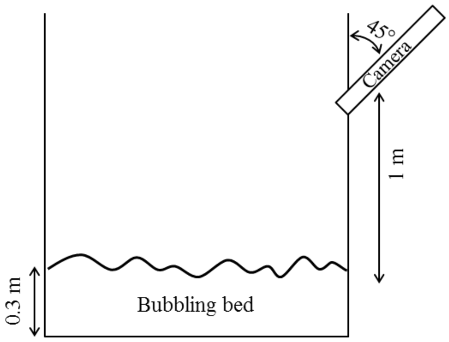

Figure 3.1: Schematic of the Chalmers gasifier with installed hot camera probe (side view)

For each recording one batch of fuel is fed into the gasifier. The investigated fuels were pellets and wood chips with batch sizes of 200 g and 80 g respectively, which corresponds to a number of particles of approximately 380 and 200. In the videos the fuel particles can be identified as dark spots on the brighter bed material background. The videos are recorded with a frame rate of 30 frames/seconds and recording is manually stopped when fuel is no longer visible as dark spots.

Table 3.2: Constant parameters for conditions in the gasifier during measurements

	Parameter	
Temperature	°C	800
Pressure	bars	1.013
Bed height	m	0.3
Bed material	µm	300
Batch pellets	g (number)	200 (380)
Batch wood chips	g (number)	80 (200)

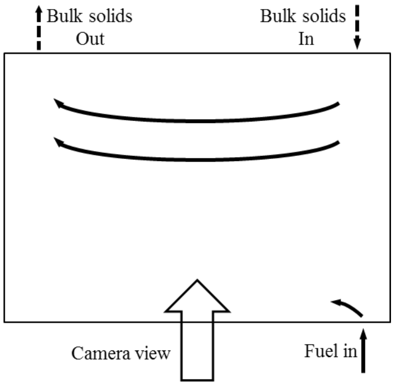

Figure 3.2: Schematic of the camera view on the bed

The view of the camera on the bed is exemplified in Figure 3.2. The solids enter in the top right, if circulation is turned on, and travel from right to left. The fuel is fed in the bottom right of the frame and is expected to spread from there over the bed towards the outlet in the upper-left corner of the frame.

3.2 Down-scaled cold flow model

The measurements with 3D particle tracking are conducted in a fluid-dynamically downscaled bubbling bed at room temperature and atmospheric pressure as it is sketched in Figure 3.3. The fluidized bed setup is assembled with three main parts: windbox, air distributor and bed chamber. The windbox is built as a hollow aluminium block, where pressurized air enters at one side, spreads in the volume and leaves through the distributor plate. A Plexiglas cube, which is screwed on the base, serves as the upper part of the bed, holding the distributor plate in place. The air distributor of the bed is a thin, perforated aluminium plate. Four different perforation configurations were tested. The air leaves the bed through an outlet in the top of the bed. As there is no recirculation in the system all bed material should stay in the bed during the measurements. However, for high gas velocities, which exceed the terminal velocity of the used particle size, a certain amount of bed material leaves the process. This amount is assumed not to influence the set bed height and is poured back into the bed after each test run.

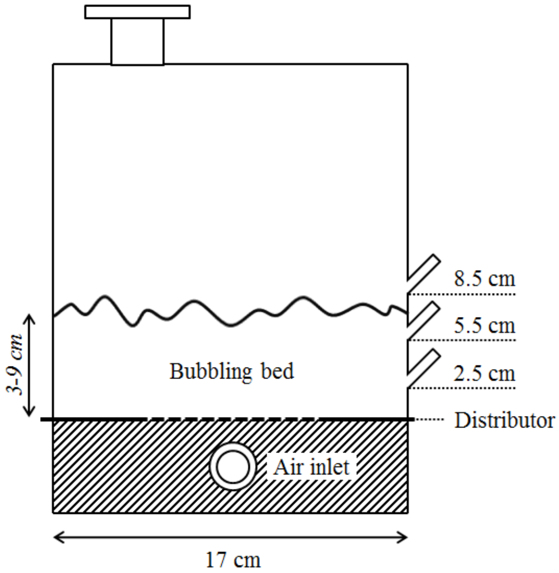

Figure 3.3: Schematic of the bubbling fluidized bed used for cold model measurements (side view)

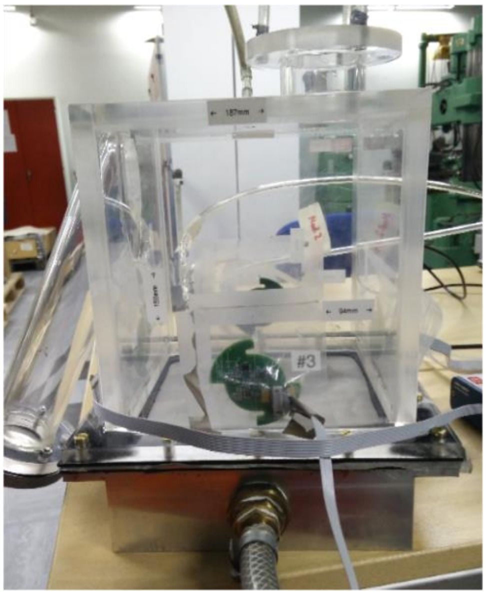

Figure 3.4: Photo of the bubbling fluidized bed used for cold model measurements (without bed material)

There are four sensor assemblies mounted on each side of the bed containing a 3-axis Anisotropic Magneto Resistive (AMR) sensor each. The sensors are powered by an external voltage source, data is acquired with the National Instruments DAQ USB-6353 and sampled with a LabView program provided from Acreo Swedish ICT AB.

Three taps on the side access the chamber for pressure measurements at different heights of the bed. The pressure measurements at the three taps plus one port located at the air inlet are performed with the National Instruments DAQ cDAQ-9178 and a voltage measuring LabView program.

The bed is fluid-dynamically downscaled applying Glickman's scaling laws [15] like it was done by Sette et al. [16], which leads to a scaling factor of 5 for length. The bed's area of 0.029 m^2 resembles therefore an up-scaled area of 0.72 m^2. All scaling parameters are summarized in Table 3.3.

Table 3.3: Parameters for hot and cold model

Parameter	Unit	Hot model	Cold model
Temperature	°C	900	20
Pressure	bars	1.013	1.013
Kinematic gas viscosity	m^2/s	$4.41\cdot10^{-5}$	$1.845\cdot10^{-5}$
Gas density	kg/m^3	0.1872	1.275
Bed material density	kg/m^3	2600	8900
Bed material particle diameter	µm	300	60
Scaling factor length	-	$5 \cdot L$	L
Design superficial velocity	m/s	$\sqrt{\frac{u^2}{5}}$	0.13
Dispersion coefficient	m^2/s	$D \cdot 5^{\frac{3}{2}}$	D

The four different distributor plates are dimensioned according to the design rules as they are found in [33] meaning that the number and size of holes is varied. An equal flow is obtained with sufficient pressure drop over the distributor and by applying the rule of thumb for industrial applications:

$$\frac{\Delta \mathrm{p_d}}{\Delta \mathrm{p_b}} = 0.2 - 0.4 \qquad (5)$$

The four distributor plates used in the measurements have a pressure ratio range between 0.11 and 9.1, where the pressure drop over the bed is constant and calculated according to Kunii and Levenspiel. [33] to be:

$$\frac{\Delta p_b}{L_{mf}} = \left(1 - \varepsilon_{mf}\right)\left(\rho_s - \rho_g\right)g \qquad (6)$$

Where L_{mf} is the bed height at minimal fluidization, ε_{mf} is the void fraction, ρ_s the solids density, ρ_g the gas density and g the gravitational force. The pressure ratios are summarized in Table 3.4 for all velocities applied later in the measurements. The distributor plates are named after the number of holes (n×n) and the holes diameter in mm.

Table 3.4: Pressure ratio at different gas velocity for different distributor design

Gas velocity (m/s)	Gas velocity up-scaled (m/s)	$\Delta p_d/\Delta p_b$ for different distributor design			
		5×5 / 2.6 mm	7×7 / 1.4 mm	9×9 / 1.1 mm	5×5 / 1.5 mm
0.04	0.07	0.11	0.12	0.13	0.47
0.07	0.14	0.27	0.34	0.38	1.29
0.1	0.20	0.57	0.70	0.80	2.72
0.13	**0.27**	**1.02**	**1.24**	**1.41**	**5.02**
0.16	0.34	1.63	2.07	2.30	7.78
0.2	0.43	2.74	3.56	3.86	9.10

The chosen four configurations allow the investigation of the influence of a wide pressure ratio on the fluidization behaviour, where a high pressure drop over the distributor is assumed to generate many small bubbles and a low pressure drop gives larger fewer bubbles. It can also confirm the assumed importance of the pressure ratio in down-scaled units, as in literature the rule of thumb in Eq. (5) is often not applied on laboratory tests. The characteristic curves of the distributors, which where obtain experimentally can be seen in Figure 3.5.

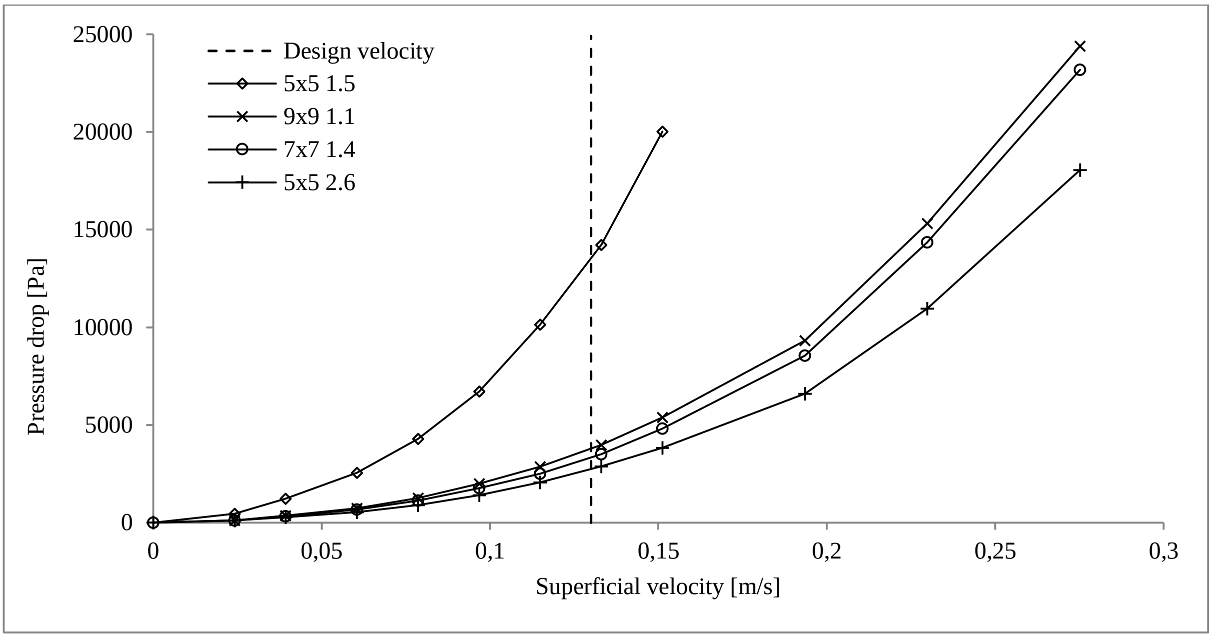

Figure 3.5: Pressure drop over the distributor plate for varying inlet gas velocity and four different distributor plates

There are two plates with 5×5 holes, one with a orfice diameter of 1.5 mm and the other with 2.6 mm, which yields to the steepest and flattest characteristic curve respectively. The plates with 7×7 and 9×9 are designed to give approximately the same characteristic curve.

4 Methodology

4.1 Hot camera probe

4.1.1 Applying image processing

As mentioned before the images obtained with the hot camera probe are processed to extract unique features for the particles. This makes it possible to track them on the bed's surface and by predicting their next detection position to maintain their identity even when they disappear from the image in certain frames.

The processing is done in Matlab, whereas the development of the used program was not part of this work. However, the consecutive tasks of the program shall be described briefly. There are numerous functions for image processing, such as video file readers, blob analysis, smoothing functions, the Kalman filter and camera calibration, already implemented in Matlab, so that they can be applied on the video measurements. Firstly the intrinsic parameters of the camera are implemented making it possible to process all images undistorted. After loading a video the Laplacian of Gaussian filter (LoG) is applied on the images, which is a filter especially helpful to stress blob structures. The form of this mask is similar to a Mexican hat (Figure 4.1), which is fitted on the size of the particle. In the middle the filter structure is very high to maximize the pixel values of the particle, while the brim has very low values to sharpen the edges. Thus the particle becomes a more salient blob, which can be distinguished better from the background.

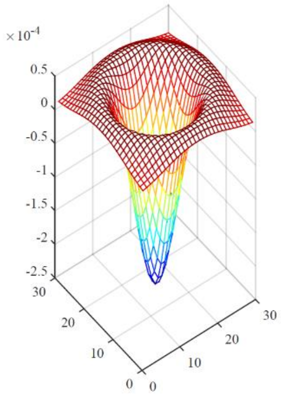

Figure 4.1: Visualisation of the Laplacian of Gaussian filter in Matlab

A section of an unprocessed image and the effect of applying the LoG can be seen in Figure 4.2a and b. The movement of the fluidized bed in the background are removed and particles are visible as light grey spots on a black background. When analysing the histogram of the filtered image (Figure 4.2c) one can see, that the highest number of points is at 0. This is the black background of the image, which can be removed including all values higher than 0. This results in the image seen in Figure 4.2d, where the particles are now clearly visible and can be easily identified by plot detection.

Particles are now assigned to an identity and followed by using a Kalman filter function. Tracks of particles which left the image for more than 30 frames (≙ one second) are deleted while newly appearing particles get assigned to new identities.

After obtaining the tracks, i.e. the position of all particles for the whole video, the information of the particles movement is available in pixel/frames and has to be translated into world coordinates (m/s). As it is not possible to place the checker board into the hot gasifier, the extrinsic parameters, i.e. the measures of the gasifier and the not changing position of the camera, can be implemented in the program instead.

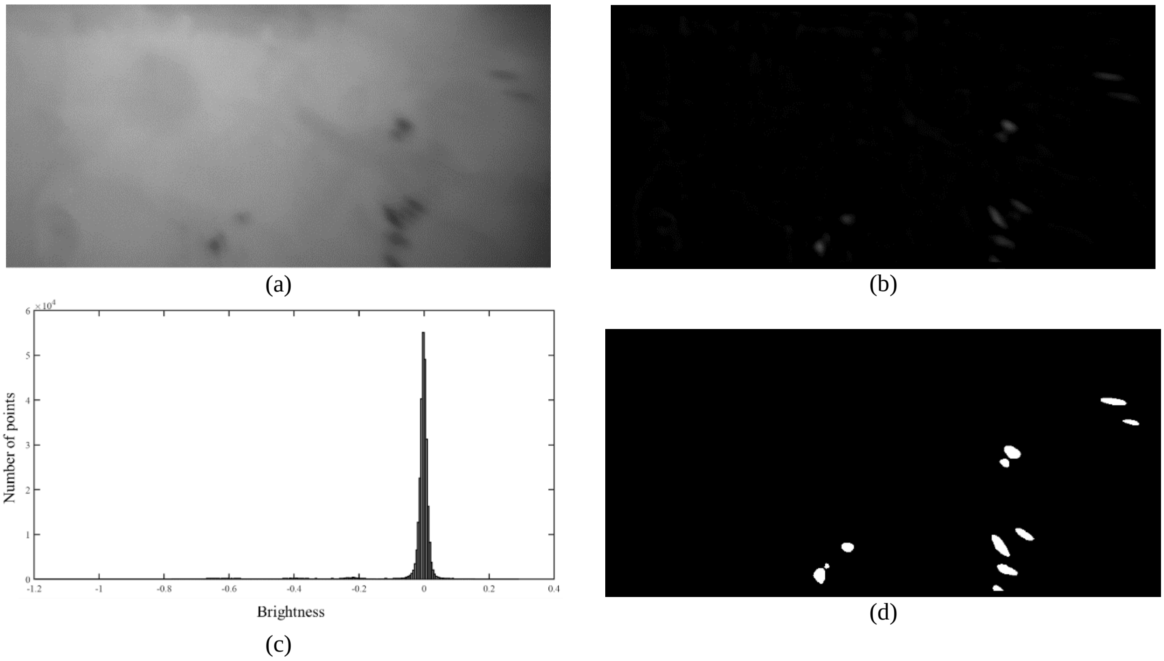
(a) (b) (c) (d)

Figure 4.2: Progress of an image of the camera measurements. (a) Original image of the gasifier. (b) Image after applying LoG function. (c) Histogram of the image after applying LoG function. (d) Image after applying thresholding.

4.1.2 Calculation of the lateral dispersion coefficient

The lateral dispersion coefficient in x-direction is defined by Einstein's equation of the Brownian motion.

$$D_x = \frac{\Delta x^2}{2\Delta t} \tag{7}$$

Here *Δx* is the distance the tracer particle travelled from one measurement position to the next and *Δt* is the time needed. The dispersion coefficient in y-direction is calculated accordingly. As mentioned before measurement positions only count if the tracer particle changes mixing cells. The dispersion coefficient is calculated as visualized in Figure 4.3, which illustrates a bed section with 6 mixing cells as it was elaborated by Sette et al. [16]. The particle starts to the very right (indicated as filled circle) and is first tracked at three other positions in the first mixing cell before it changes to a new cell to the left. Movement within a single mixing cell is marked with dashed arrows and is not taken into account for calculations of the lateral dispersion coefficient, while a change of cell is marked with thin solid arrows. Eventually the dispersion coefficient is calculated with the distance between the first observation in the first cell and the first in the new cell, marked with a thick solid arrow.

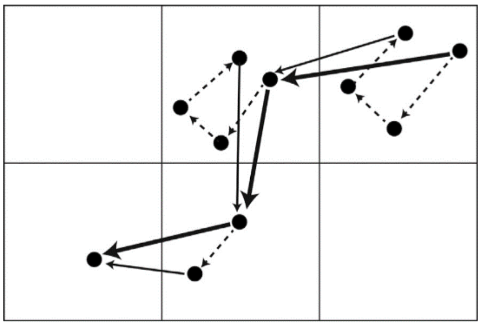

Figure 4.3: Calculation of lateral dispersion coefficient from a single particle in a bed with 6 mixing cells by Sette et al. [16]

4.2 3D particle tracking

4.2.1 Measurement method

One aim of the work is to start up the newly developed experimental setup, wherefore the combinations of three different bed parameters are examined to get a good insight into the system and be able to define general conditions for further usage.

For the measurements the following three parameters are varied:

1. Pressure drop (4 distributor plates with varying number of holes and size)
2. Bed height (3.0/5.0/7.0/9.0 cm)
3. Inlet gas velocity (from 0.04-0.2 m/s, see also Table 3.4)

The design conditions for the setup are a gas velocity of 0.13 m/s and a bed height of 7 cm. Each combination of the three parameters is measured with a sampling rate of around 20 Hz. The resulting time step of 0.05 s is much longer as the time needed for a possible reset of the sensor, if the magnetic tracer comes too close. Thus the S/R is controlled by the measurement program, i.e. S/R is performed after each sample and does not affect the measurements. For higher sampling frequencies the S/R is done previous to the program start, but cannot be performed during sampling. This implies the risk that the magnetic tracer comes too close and a sensor, i.e. three sensing elements, is saturated and therefore out of order for the rest of the measurement. Then again as the position of the tracer is calculated as a minimization problem including information from all four sensor sets, all following measuring points after the saturation of one set are unusable. For these cases the time of saturation has to be identified and the points afterwards have to be removed before processing the data.

Some conditions are measured at a sampling rate of 100 Hz to compare the accuracy of the measurement method, which with a low measuring frequency is considered to be critical for higher inlet gas velocities. However, the problem explained above yields to very short measurement times as the higher the gas velocity the higher is the risk of saturation of a sensor and measurement points have to be removed.

All three parameters combined with each other result in 96 different conditions. Most measurements at the three lowest levels of velocities are measured over 1 hour with the tracer magnet moving freely inside the bubbling bed. Experiments around and above the gas velocity of 0.13 m/s are measured for 15 min to avoid a major loss of bed material through the top outlet. For every measurement before inserting the tracer magnet into the fluidized bed a background measurement is performed, while fluidization is already ongoing. This data is used to reduce noise and the influence of surrounding magnetic disturbance, when the measurement is processed later.

Solving the minimization problem of Eq. (4) with the measurements from 12 sensing elements is time consuming and therefore done offline. After processing the data the tracer magnets position and orientation is obtained and saved for further analysis. The data from the pressure measurements is not included in the processing of the data from the AMR sensors, but is done separately.

4.2.2 Calculations for evaluation

Further analysis included the evaluation of velocity of the tracer magnet at every position measured. The velocity was calculated as the following

$$\boldsymbol{v_{i+1}} = (\boldsymbol{p_{i+1}} - \boldsymbol{p_i}) \cdot f \tag{8}$$

Here $\boldsymbol{v}$ is the velocity vector at i+1, $\boldsymbol{p}$ the position vector at the i$^{\text{th}}$ measurement point and $\boldsymbol{f}$ the sampling frequency of the measurement. The velocity of the very first measurement point is assigned to be zero. The magnitude of the velocity at a measurement point is then calculated as

$$|\boldsymbol{v}| = \sqrt{v_x^2 + v_y^2 + v_z^2} \tag{9}$$

To obtain information about flow structures, the whole bed is discretized into a mesh of bins with the size of 1×1×1 cm. In every bin an average velocity was calculated as

$$\bar{v}_x = \frac{\sum\left(v_{x_1} + v_{x_2} + v_{x_3} + \cdots + v_{x_n}\right)}{n} \tag{10}$$

Here $\bar{v}_x$ is the x-component of the average velocity in a bin with n measurement points. The y- and z-components are calculated accordingly. To make vector fields of the velocities visible the 3D graph can be sliced along the x- or y-direction and each slice is plotted as a field separately (examples in 5.2.2 and following). For the plotted vectors only the y and z-components (respectively x and z-components) are used. The vectors are normalized and further the velocities in positive z-directions are indicated with a red background colour, while the velocities in negative z-direction are marked in blue. The intensity of the colour indicates the magnitude of the z-component of the velocity.

Most results showing distribution curves are plotted as probability density function (PDF) to achieve better comparability between measurements with large difference in number of measurement points. The PDF is defined as the following

$$P(a \leq X \leq b) = \int_a^b g(x)dx \tag{11}$$

Here P is the so-called probability measure, a function returning a probability for every event in a defined probability space of an experiment, X is a real random variable and g is the probability density function. In graphs showing distribution curves the measurement points are plotted as histograms and the PDF can be calculated by dividing the left side of Eq. (11) by the area given by integral on the right side.

4.2.3 Procedure for particles trapped in corners and bottom region of the bed

Especially for long measurements, i.e. duration of 1 h, and low inlet gas velocities the magnetic tracer spends significant time at the bottom and in the corners of the bed. The measurement points taken during this time distort the results, e.g. comparability of particle distribution over the whole bed of measurements with different duration time. Large numbers of measurement points of the particle which is getting trapped in corners/bottom of bed (later referred to as “trapped particles”) are therefore removed by the following criteria

$$|\boldsymbol{p}_{\boldsymbol{i+1}} - \boldsymbol{p}_{\boldsymbol{i}}| < T \cdot \frac{v_{gas}}{f} \tag{12}$$

Here v_{gas} is the inlet gas velocity and T the threshold, a number between 0 and 1 which can be chosen by the user depending on how distorting the stuck particles are conceived. For the result of this work the threshold was chosen to be 0.7.

4.2.4 Calculation of lateral dispersion coefficient

In principle the lateral dispersion coefficient from the 3D measurements should be obtained similarly as it was described in the section 4.1.2. Again the presence of mixing cells is a requirement and as in this case the information about the tracer particles' movement is available continuously and in all 3 dimensions the mixing cells in every measurement can be identified directly with the help of the velocity fields. Even flow structures with fully established bubble paths are always observed in connection with 2×2 mixing cells, wherefore only the dispersion coefficients for these measurements are evaluated.

However, the lateral movement (in for example x-direction) in such a small bed is rather limited and in the physical bed the tracer particle can just move from one mixing cell to the other and backwards. Thus, the bed walls limit the *Δx* used in Eq. (7) strongly, resulting in very small values for *D*. To remove these wall effects from the calculation the bed is virtually expanded to an infinitive bed, where the tracer particle moves without boundaries. This is done by defining the positions of the two mixing cells, i.e. the border between the cells, from the experimental data and thereafter obtaining the number of valid crossings of the tracer over this border for the whole measurement (see explanation of valid crossing below). Now, to find the mixing cell in which the tracer particle would have ended up, if it was moving in an infinitive bed, the total number of crossings are used in a Monte Carlo experiment (Figure 4.4).

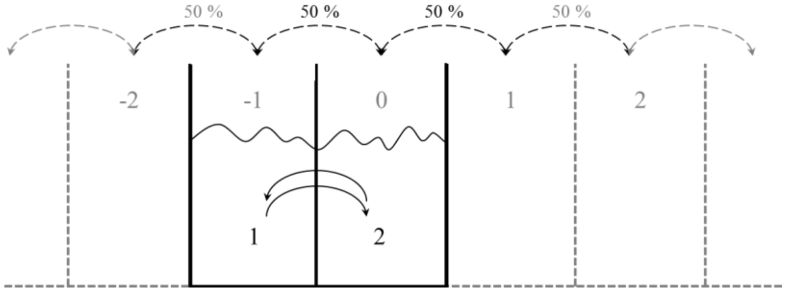

Figure 4.4: Bed expansion according to Monto Carlo method.

In reality the bed consists of two mixing cells (indicated with black numbers) and the tracer can only move into one direction (100 %). In the virtual bed the particle can either move left or right (50/50 %), thus to obtain the end position in a bed expanded on both sides, the number of crossings obtained from the measurement, N, has to be doubled, i.e. 2×N, in order to account for the physical limitation that the bed walls put on the tracer movement during the experiments. The domain for the Monte Carlo experiment is now defined. The tracer has two options:

1) Jump to the cell to the left →50 % probability to end up in *-1*
2) Jump to the cell to the right → 50 % probability to end up in *1*

As explained above, this lottery is done for 2×N jumps and the *Δx* from the Monte Carlo experiment is calculated as:

$$\Delta x = w_{cell} \cdot p_{end} \tag{13}$$

Here w_{cell} is the width of the mixing cell obtained from the measurement and p_{end} is the final cell of the tracer after moving according to the Monte Carlo experiment. If repeating the experiment for a high number of times, the distribution of the resulting *Δx* will be a normal distribution peaking at 0. Finally, the lateral dispersion coefficient is calculated with the mean of the absolute values of *Δx* and the *Δt* equal to the total time of the jumping tracer.

Further, the border between the two real mixing cells was defined beforehand, but not every crossing over this border is assumed to be a “valid crossing”. For example if the particle gets trapped and jumps back and forth over the border, this change of mixing cell does not contribute to the macroscopic mixing in the bed. Therefore, as a valid cell change only the crossings after which the tracer travels at least to the region of the rising bubble path are counted.

5 Results and discussion

5.1 Hot camera probe

The lateral dispersion coefficients for different inlet gas velocities for the measurements at hot conditions in the Chalmers gasifier are shown in Figure 5.1. The coefficients are here plotted against the excess gas velocity, which is the difference between the superficial gas velocity and the minimum fluidization velocity. The velocity of minimum fluidization is 0.022 m/s for the used bed material in the gasifier. The range of the velocities measured in the down-scaled cold model are indicated in grey.

The lateral dispersion coefficient is increasing linearly with increasing excess gas velocity, which is expected when comparing with values in literature [7], [16], [24]. The results for pellets and wood chips are very similar, however the increasing gas velocity has a slightly stronger effect on the dispersion coefficient of the pellets.

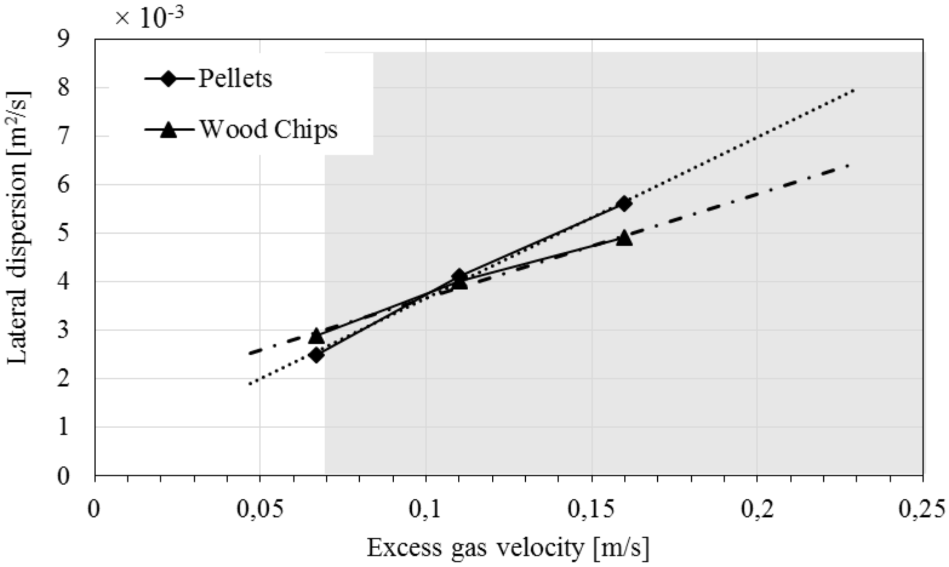

Figure 5.1: Dispersion coefficient with increasing excess gas velocity

5.2 Down-scaled cold model

5.2.1 Robustness of the measurement method

As the measurement method is newly implemented in the experimental setup, the robustness of the method has to be evaluated. The first measurements are done at a sampling frequency of 20 Hz as this allows a sampling with continuous S/R and each condition is measured for one hour. To evaluate if this sampling rate is sufficiently high, a measurement with the distributor plate with 7×7 holes and a hole diameter of 1.4 mm (7x7 1.4) at bed height of 5 cm and a gas velocity of 0.1 m/s is repeated at 100 Hz. Figure 5.2 shows the PDF of the height distributions of both measurements, where the 100 Hz measurement is displayed in different frequencies. To get the 50 Hz curve every other measurement point was saved and evaluated separately, thus for the 20 Hz and the 10 Hz curve every fifth and tenth point is taken respectively. Finally, the height distribution of the original 20 Hz measurement is plotted in the same graph. As seen in the figure all lines show the same trends and peak at a bed height of around 0.8 cm, which means that the sampling frequency is sufficiently high for evaluating the height of particles within the bed. The peak indicates trapped particles and the much higher maximum of the original 20 Hz measurement can be explained with the long measurement time of about 1 h, whereas the 100 Hz measurement had a duration of only 15 min (compare Appendix A.1).

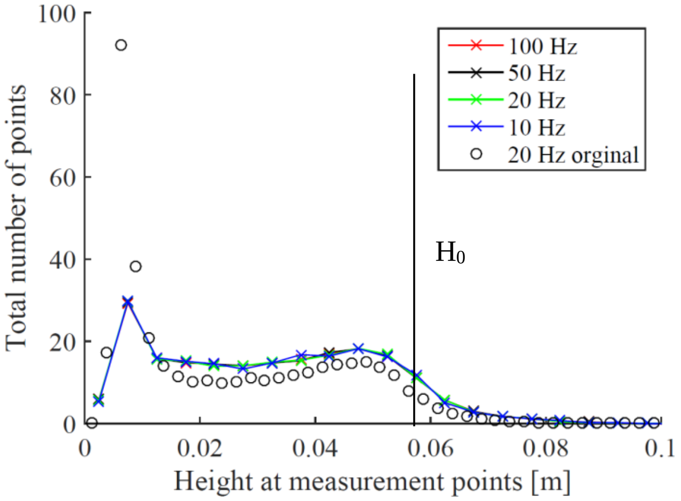

Figure 5.2: Height distribution (PDF) of two measurements sampled at 20 Hz and 100 Hz respectively, with the 7x7 1.4 plate at a bed height of 5 cm and a gas inlet velocity of 0.1 m/s. H_0 = dense bed height.

Figure 5.3 is constructed similarly to Figure 5.2, but shows the PDF of the velocity magnitude instead. As before the curve show the same trends for all frequencies and both measurements. However, the peaks of the curves vary significantly when decreasing in frequency and is highest for the original 20 Hz measurement. The maxima not only increase, but also the location of the maxima moves to the left of the graph, i.e. to lower velocities. By removing the trapped particles of the 20 Hz measurement the maximum of the curve moves to the right and ends up at a similar velocity as the maximum of the 20 Hz curve of the 100 Hz measurement, but does not decrease (compare Appendix A.2). The graph indicates that for accurate velocity measurements the sampling rate has to be increased. As the 100 Hz curve and the 50 Hz curve are closer to each other than the following curves, one can assume that a measurement frequency of 50 Hz might be sufficient for this gas velocity. Further, a longer measurement time is not necessarily beneficial for the quality of the data, because it influences the distribution of the velocity by increasing the time the tracer can be trapped, thus the number of measurement points with very low velocities. This should be considered for further improvement of the measurement system.

The uneven slope of the curves from the 100 Hz measurement can be explained with a rather low number of total measurement points, which is decreased to around 19k due to sensor saturation later in the measurement.

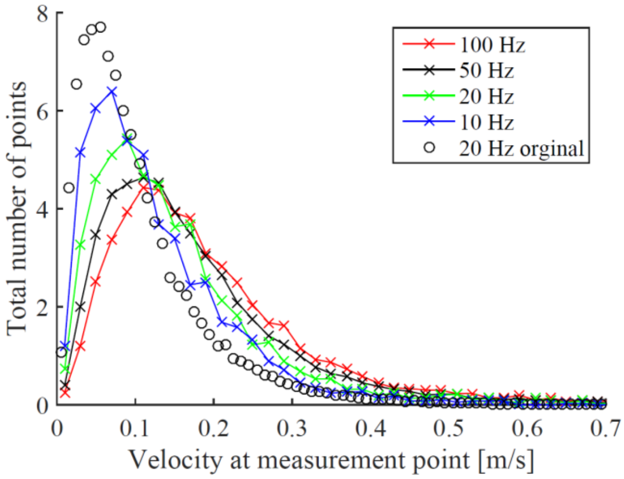

Figure 5.3: Velocity distribution (PDF) of two measurements sampled at 20 Hz and 100 Hz respectively, with the 7x7 1.4 plate at a bed height of 5 cm and a gas inlet velocity of 0.1 m/s.

The optimal measurement time is evaluated, wherefore different parts of the 20 Hz measurement are compared with each other. Figure 5.4 shows the PDF of the height distribution for a total measurement time of 60 min compared with the first 30, 15 and 7.5 min. All four curves have the same trends and peak at a height of about 0.7 cm. The graph indicates that the original measurement time of 1 h can be shorten drastically. Further measurements are therefore performed over 15 min instead.

Further, the effect of applying the policy for trapped particles is evaluated. As can be seen in Figure 5.5 the peak of the curve is reduced drastically. The figure shows the same results as in Figure 5.4, but after applying the criteria of Eq.(12), where 41.8 % of the measurement points are removed (see also Appendix A.1 and A.2).

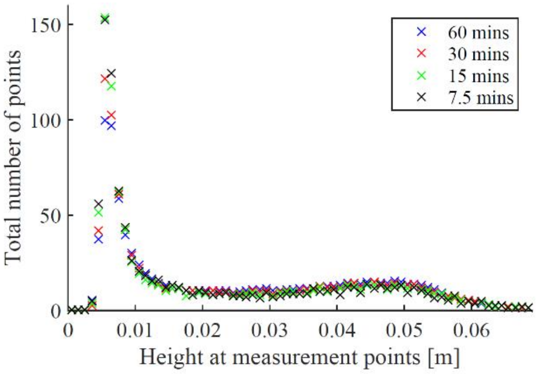

Figure 5.4: Height distribution (PDF) of measurement sampled at 20 Hz for around 60 min with the 7x7 1.4 plate at a bed height of 5 cm and a gas inlet velocity of 0.1 m/s.

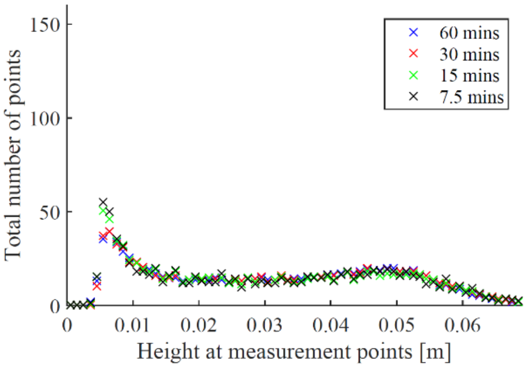

Figure 5.5: Height distribution (PDF) of measurement sampled at 20 Hz for around 60 min with the 7x7 1.4 plate at a bed height of 5 cm and a gas inlet velocity of 0.1 m/s after removing trapped particles.

Where the trapped particles are mostly removed can be seen in Figure 5.6 and Figure 5.7. To display the particle distribution over the entire bed the bed is discretized into a mesh of bins with the size of

1x1x1 cm. For every 1 cm thick slice (in the x-y-plane) the distribution is plotted as a coloured 2D histogram with a maximum number of particles of 150 (red in the colour bar). The plots reflecting a similar distribution as seen before with large amounts of particles trapped in the lowest plane, where most of the particles are removed, and the second maximum between a height of 0.04 and 0.06 m.

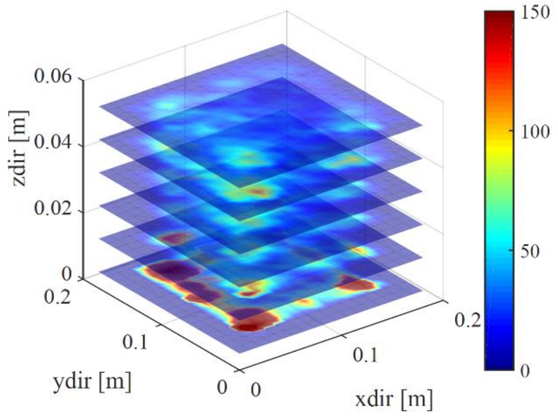

Figure 5.6: Particle distribution of measurement sampled at 20 Hz for around 60 min with the 7x7 1.4 plate at a bed height of 5 cm and a gas inlet velocity of 0.1 m/s.

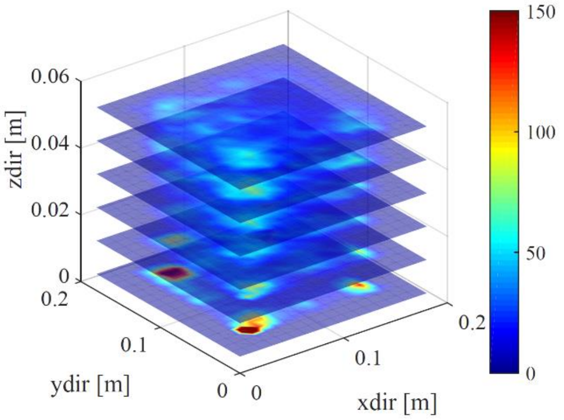

Figure 5.7: Particle distribution of measurement sampled at 20 Hz for around 60 min with the 7x7 1.4 plate at a bed height of 5 cm and a gas inlet velocity of 0.1 m/s after removing trapped particles.

After evaluating the robustness of the measurement system, the results are considered to be efficiently accurate for the purpose of further evaluation. In a next step flow structures in the bed are identified and the influence of the three parameters varied in the measurements are discussed.

5.2.2 Influence of the fixed bed height on flow structures

The pressure drop over the fluidized bed is dependent of the height of the fixed bed (see Appendix A.3 with pressure measurements between the port at 2.5 cm and the one at 8.5 cm (Figure 3.3)). The pressure drop increases linearly with increasing fixed bed height, and seems in combination with the used geometry of the setup to have an influence on how flow structures are established in the bed. In a high bed bubbles rise and grow over a longer distance, thus, become larger wherefore broader bubble paths are formed. In combination with the given bed geometry this results in a fewer number of bubble paths. On the contrary a low bed yields higher number of bubble paths. This tendency can be obtained when plotting vector fields with the average velocities over the whole bed as it was explained in the section 4.2.2, where an examples is seen in Figure 5.8. Note that the velocities of the upwards movement are much higher (around a factor of 10) than the velocities of the downwards movement. To make both visible in the plot the intensity of the red colour in the colour bar increases slower that the blue colour decreases. Further, the numbers on the colour bar are not equal to velocity in m/s, but the colours are defined so that the highest positive z-component of all average velocities in the bed is set equal to 1 and the shading is adjusted accordingly.

For a fixed bed height of 3 cm there is a trend to form around 3 bubble paths (and up to 5 paths are possible), as it is shown in Figure 5.8. However, the relatively small cross sectional area of the bed seems to limit the establishment of smooth flow structures over the whole bed like they were described in section 2.3. For most measurements in the 3 cm fixed bed the velocity fields are therefore unstructured while showing nevertheless much movement.

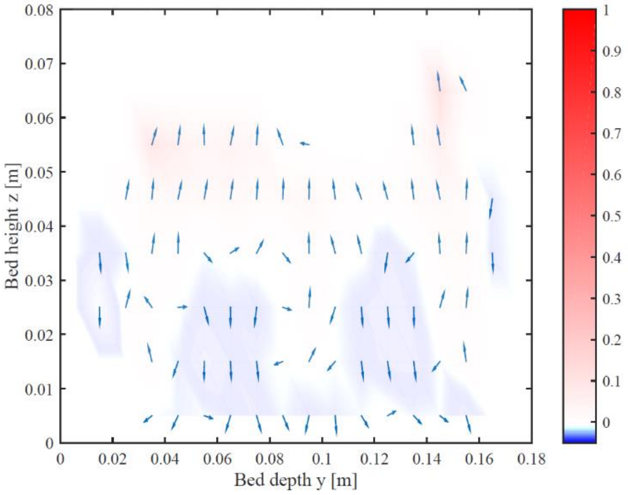

Figure 5.8: Flow structure of the slice 0.09-0.1 m in x-direction, measured with the 9x9 1.1 plate at a bed height of 3 cm and a gas inlet velocity of 0.13 m/s. Colour bar indicates magnitude of z-direction of the velocity.

The bed height of 5 and 7 cm seems to be ideal to form two bubble paths, where two paths are considered to be the optimal for the given bed geometry, as when they occur the flow structures are often even and fully established. Figure 5.9 visualises even flow structures with two well established bubble paths for a bed height of 5 cm and an inlet gas velocity of 0.13 m/s. The structures are similar for all four distributor plates.

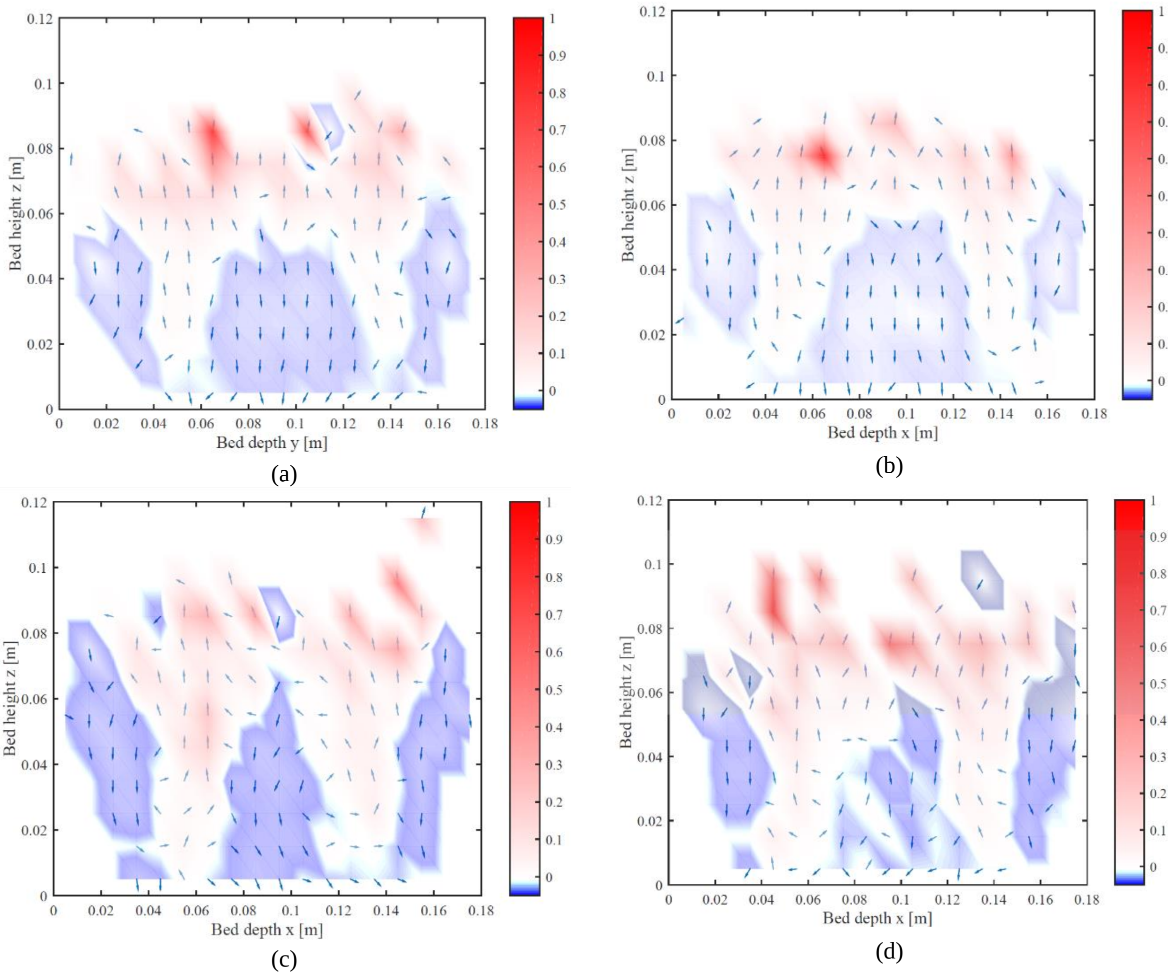

(a) (b)

(c) (d)

Figure 5.9: Flow structures of different slices measured at a bed height of 5 cm and a gas inlet velocity of 0.13 m/s. Colour bar indicates magnitude of z-direction of the velocity. (a) 5x5 1.5, slice 0.09-0.1 m in x, (b) 9x9 1.1, slice 0.1-0.11 m in y (c) 7x7 1.4, slice 0.11-0.12 m in y, (d) 5x5 2.6, slice 0.06-0.07 m in y.

The same comparable flow structures for all distributor plates are obtained in the bed height of 7 cm, but occur at an inlet gas velocity of 0.1 m/s. It shall be mentioned at this point that although the pressure drop over the four distributors is very different (for a velocity of 0.13 m/s varying from 27.39 to 137.37 mbar), still the two-bubble-path pattern is very clear and similar. The fixed bed heights of 5 and 7 cm are therefore assumed to be ideal to establish even flow structures in the given geometry.

Moreover, the bed height of 9 cm is for high velocities to problems for the given geometry of the setup. The bubbles grow very tall and large eruptions ending up at the devices top. The volume for the freeboard is too small so that the movement of the bed material and the tracer particle is hindered and measurement results are assumed to be influenced negatively. This is visible as very broad bubble paths, wherefore often only one path is established in the velocity field.

5.2.3 Influence of the inlet gas velocity on flow structures

For all bed heights and distributor plates the lowest inlet gas velocity of 0.04 m/s is too low to establish flow structures. This results in the tracer particle being trapped in one corner on the bottom or some movement along the bottom plane, but none in vertical direction. With increasing inlet gas velocity the pressure drop increases as shown in Figure 3.5, however the presence of bubble paths and even flow structures are not directly linked to the pressure drop over the distributor plate, but more to the inlet gas velocity itself. This is concluded when comparing the velocity fields showed in Figure 5.9. As mentioned before, although there is a different in pressure drop for the four distributor plates the flow structure are similar.

The inlet gas velocities of 0.1 and 0.13 m/s seem to be optimal to establish even flow structures with two bubble paths. For higher velocities the bubble paths become broader and the area where particles have space to sink in the middle of the two paths gets narrower. For the two distributor plates with the higher pressure drop (5x5 1.5 and 9x9 1.1) and bed heights of 7 cm and higher the paths grow together and form a single rising paths centred in the middle of the bed with increasing velocity.

This tendency is visualised in Figure 5.10. In (a) for an inlet gas velocity of 0.07 m/s the sinking particles in the middle and on the sides are slower (light blue). The blue area in the middle is broader and reaches from the bottom to a height of around 0.07 m. The graph in (b) is taken from a measurement with an inlet gas velocity of 0.13 m/s. Velocities of rising and also sinking particles are higher. The areas are stretched in z-direction meaning that the tracer particle reaches higher in the bed, which is reasonable for a higher gas velocity. The area in the middle of the two bubble paths is reduced by around ½ and the bubble paths grow broader (see e.g. at the height of 0.08 m). The last figure (c) is taken for an inlet gas velocity of 0.2 m/s. The blue area in the middle is further reduced and the bubble paths are very broad up from a height of 0.07 m. The freeboard is increasing in volume and the tracer particle spends most likely more time above the dense bed.

Also for trapped particles the inlet gas velocities of 0.1 and 0.13 m/s are optimal. Here the number is lowest, while it often increases slightly for 0.16 and 0.2 m/s.

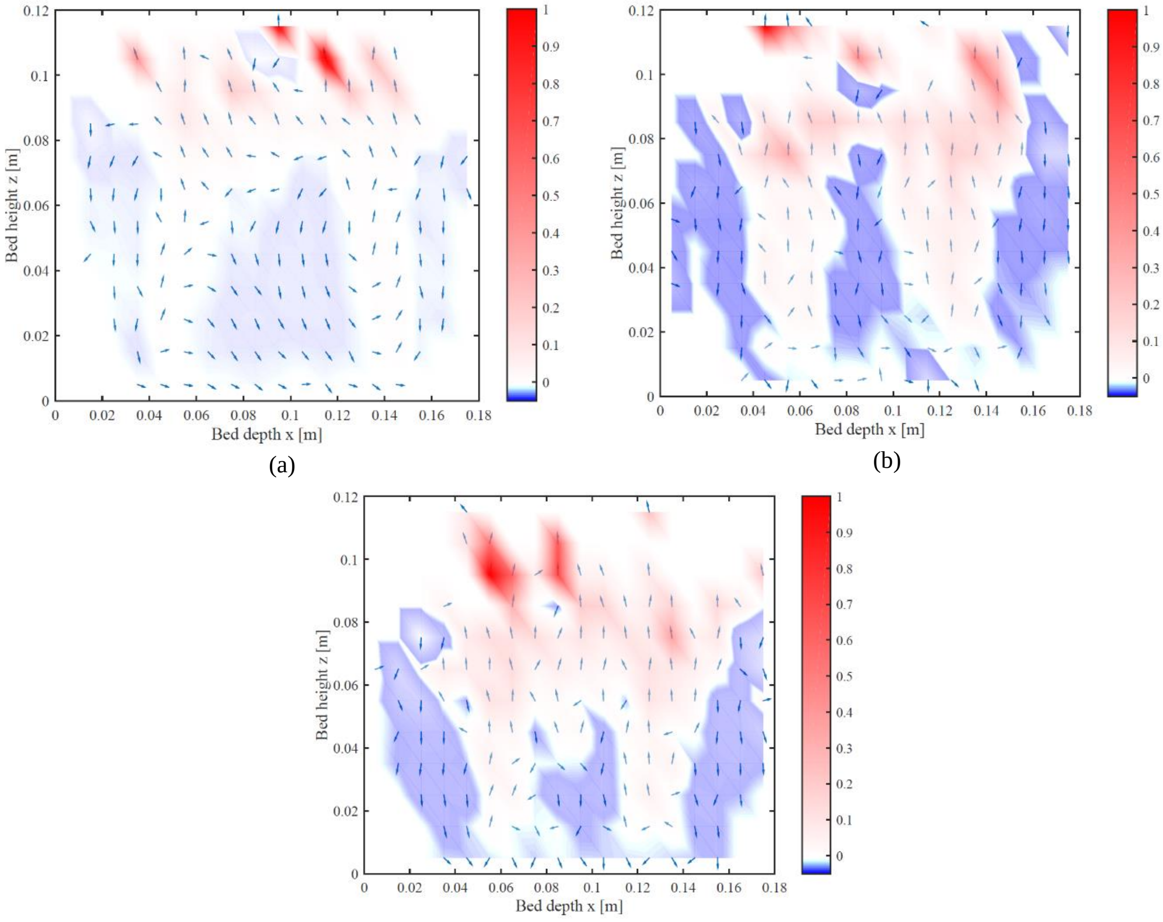

(a) (b)

(c)

Figure 5.10: Flow structures of different slices measured with the 5x5 2.6 plate at a bed height of 7 cm. Colour bar indicates magnitude of z-direction of the velocity. (a) 0.07 m/s, slice 0.1-0.11 m in y, (b) 0.13 m/s, slice 0.11-0.12 m in y, (c) 0.2 m/s, slice 0.11-0.12 m in y

5.2.4 Influence of other factors

The design of the distributor plates, i.e. the placement of the holes is not optimal. The holes seem to be too far away from the bed walls as there are large parts of trapped particles on the sides.

The air from the inlet distributes uneven over the area of the bed, which results in unsymmetrical particle distribution over the whole bed. The effect can be seen when the bed is fluidized as bubbles appear first on one half of the bed.

5.2.5 Lateral dispersion coefficient

As the calculation method of the lateral dispersion refers to the presence of fully established bubbled path, the coefficients are only calculated for cases with 2×2 mixing cells. All calculated values for the dispersion coefficient in x- and y-direction can be obtained in Table 5.1. All values are up-scaled to results in a hot bed. The conditions were less or more mixing cells are established, for which it is not possible to evaluate the dispersion coefficient are marked with “x”. As can be seen in the table, the conditions of the distributor plates with the two lowest pressure drops (7×7 1.4 and 5×5 2.6) are optimal for even flow structures in the given geometry. Further, only the bed heights of 5 and 7 cm (0.25 and 0.35 m in up-scaled hot bed) are suitable. For the other two distributor plates (9×9 1.1 and 5×5 1.5) the coefficients can only be calculated for low gas velocities. Figure 5.11 shows the development of the lateral dispersion coefficient in y-direction for the 5×5 2.6 plate (A) and x-direction for the 7×7 1.4 (B) plate, respectively, versus the excess gas velocity. As expected the values are increasing with rising gas velocity. The values are plotted for a fixed bed height of 0.25 and 0.35 m. However, no significant difference of the dispersion coefficients can be obtained for these two heights. A reason for this might be that the chosen bed heights are lying to close to each other. The effect of fixed bed height on the dispersion coefficient can therefore not been obtained for the given setup. Figure 5.11(C) shows, the effect of the increased slope of the pressure curve (see Figure 3.5) over the distributor plates on the lateral dispersion coefficient. A steeper curve results in slightly higher values of the dispersion coefficient.

Table 5.1: Overview of up-scaled (hot) values for the lateral dispersion coefficient

Bed height (m)	Excess velocity (m/s)	5×5 / 1.5 D_x ($\times10^3$)	9×9 / 1.1 D_x ($\times10^3$)	7×7 /1.4 D_x ($\times10^3$)	5×5 / 2.6 D_x ($\times10^3$)	5×5 / 1.5 D_y ($\times10^3$)	9×9 / 1.1 D_y ($\times10^3$)	7×7 /1.4 D_y ($\times10^3$)	5×5 / 2.6 D_y ($\times10^3$)
0.25	0.20	3.06	2.05	3.21	4.02	3.24	1.89	2.64	4.67
0.25	**0.27**	4.87	3.77	8.24	7.14	4.42	3.31	11.26	8.07
0.25	0.34	x	x	11.87	13.32	x	x	14.17	12.89
0.25	0.43	x	x	15.61	x	x	x	15.26	x
0.35	0.14	2.35	x	x	1.93	4.02	x	x	1.12
0.35	0.20	5.75	3.13	6.64	4.41	7.52	2.46	7.43	5.19
0.35	**0.27**	x	x	8.12	7.78	x	x	8.90	8.41
0.35	0.34	x	x	11.31	10.65	x	x	11.18	9.89
0.35	0.43	x	x	13.60	x	x	x	18.01	x

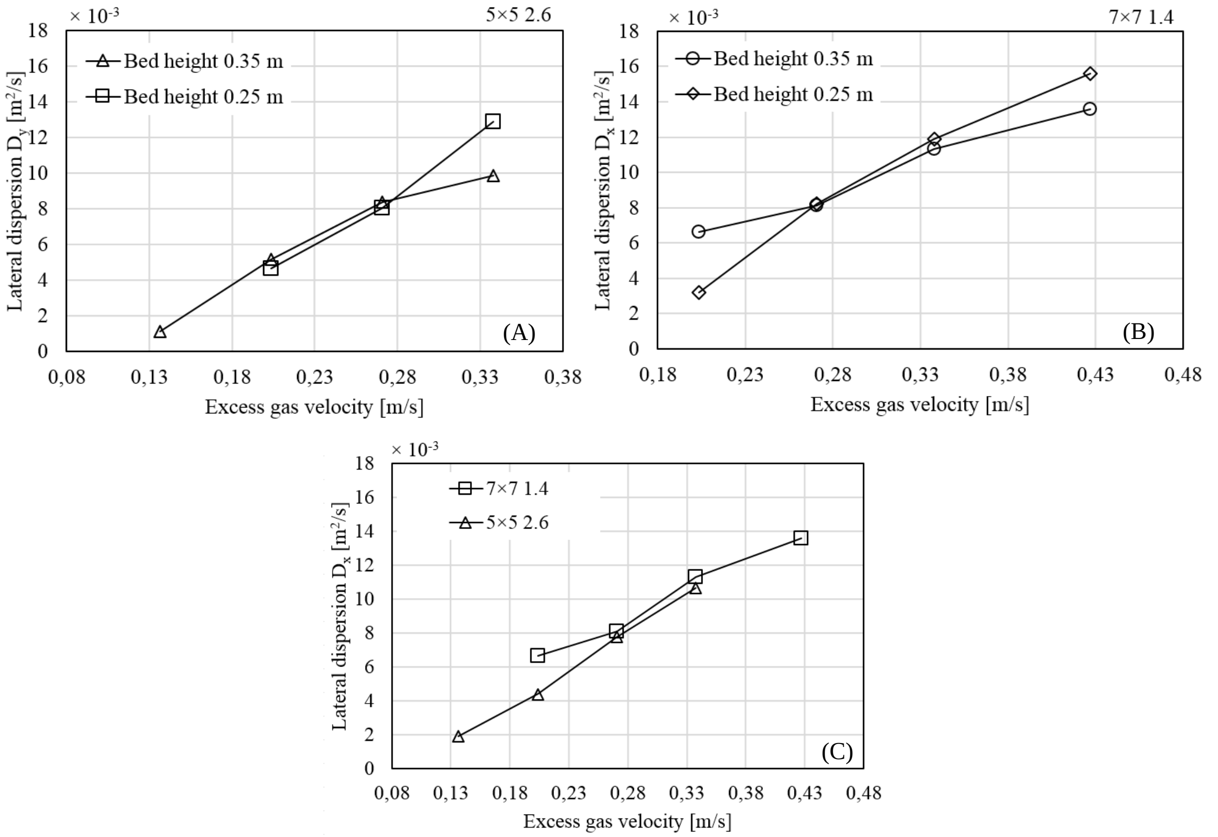

Figure 5.11: Up-scaled (hot) lateral dispersion coefficient for increasing excess gas velocity. (A) D_y with 5×5 2.6 distributor for bed height of 0.35 and 0.25 m. (B) D_x for 7×7 1.4 distributor for bed height of 0.35 and 0.25 m. (C) Bed height of 0.35 m comparing 5×5 2.6 and 7×7 1.4 distributor plates.

5.3 Comparison of both methods

Figure 5.12 shows the results of the calculation of the lateral dispersion of the present work in comparison with values obtained from the literature as well as the result from the measurements in the hot gasifier. Values are given in hot up-scaled conditions. Although the values spread over several orders of magnitude, there is a tendency of increasing dispersion with increasing bed cross-sectional area. The measurements from the hot camera probe yield to values of the same order of magnitude as the values of the down-scaled cold model, which approves the reliability of the scaling method as well as the measurement and analysis methods used in the present work. Literature values for lateral dispersion, which were obtained in very small beds without applying fluid-dynamic scaling are obviously different from the values obtained from industrial sized beds and have to be treated with caution. The comparison approves that scaling with fluid-dynamic scaling rules is essential to be able to retain conditions as they are present in industrial hot fluidized beds.

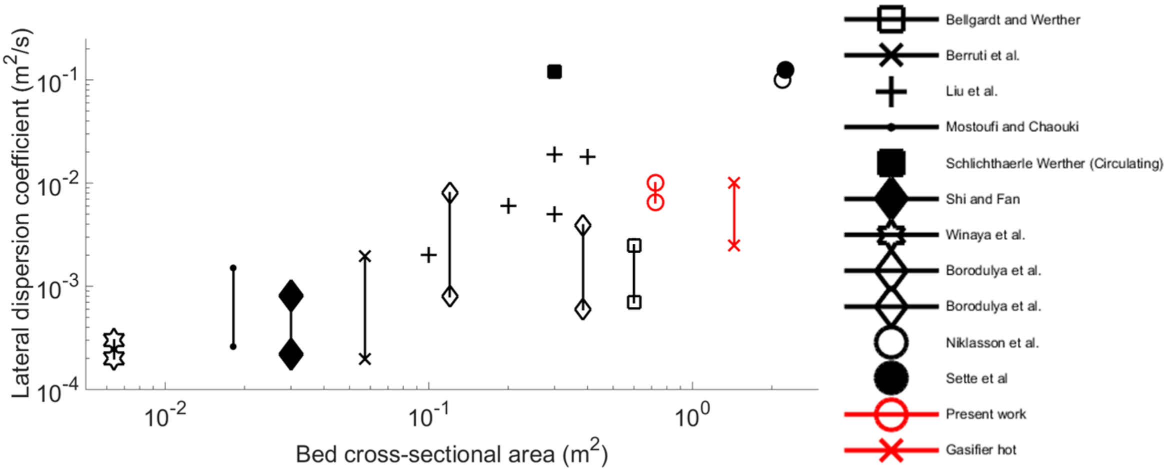

Figure 5.12: Lateral dispersion coefficient from literature by courtesy of Sette et al. [16] in comparison with values from measurements with 3D particle tracking (Present work) and hot camera probe (Gasifier hot)

6 Conclusion and suggestions for future work

In the present work the newly implemented 3D tracking system is successfully tested and experimental work is conducted and analysed. First measurements are done with a sampling frequency of 20 Hz over 60 min duration time. A first analysis of the robustness of the system shows that 20 Hz is not high enough to measure the particle’s velocity with sufficient accuracy. It can be assumed that 50 Hz is sufficiently high for a gas inlet velocity of 0.1 m/s (downscaled) and below. The accuracy was not proven for higher gas velocities. Although the experiments are done with only a single tracer magnet the measurements give statistically expected distribution of many fuel particles moving in a fluidized bed. The measurement time can be reduced to 15 min without changing the statistical results.

By applying a procedure for measurement points where the particle is trapped, which removes measurement points with very low velocities flow structures become better visible. The presence of mixing cells and flow structures in a bubbling fluidized bed can be visualized in 3 dimensions. The establishment of bubble flows is showing expected trends like increasing size of bubbles with increasing bed height and velocities.

A method to calculate the lateral dispersion coefficient is developed, where wall effect are removed in terms of expanding the bed virtually to both sides. The dispersion coefficients are calculated for all cases with 2×2 mixing cells and the values show expected trends. The values could be compared to an industrial scale hot model and show sufficient agreement. The analysis method should be further improved, whereas a first step is to investigate the sensitivity of the dispersion coefficients on the size of the mixing cells.

The setup used in the present work is the first implementation of a 3D magnetic particle tracking system in a downscaled FB to investigate mixing mechanisms and lateral dispersion in conditions similar to industrial FBs. However, the used fluidized bed is very small and limited (only 2×2 mixing cells established), wherefore further development of the measurement method to be able to use it in a bigger bed is planned. The distance in which the sensors track the magnetic tracer with sufficient accuracy can be enlarged by increasing the number of sensors. Different placement of the sensors is considered. So far the system is limited to a sampling rate of 20 Hz, if S/R is done continuously to avoid that the measurements get invalid with saturated sensors. As the time for S/R technically cannot be reduced the measurement method has to be slightly adjusted, where one solution is to increase the number of sensors and continuously reset the sensors one after each other.

7 References

1. IEA, I.E.A., *Renewable Energy Outlook*, in *World Energy Outlook 2013*, I.E. Agency, Editor. 2013. p. 197-229.
2. Ehnberg, J., Y. Liu, and M. Grahn, *Systems Perspectives on Renewable Power* B. Sandén, Editor. 2014, Chalmers University of Technology Göteborg.
3. Wahlund, B., J. Yan, and M. Westermark, *Comparisons of CO2-Reducing Alternatives for Heat and Power Generation: CO2-Capture and Fuel Shift to Biomass.* Greenhouse Gas Control Technologies, Proceedings of the 5th International Conference on Greenhouse Gas Control Technologies, 2000. **5**: p. 229-234.
4. Bhattacharya, A. and A. Datta, *Effects of supplementary biomass firing on the performance of combined cycle power generation: A comparison between NGCC and IGCC plants.* Biomass and Bioenergy, 2013. **54**(0): p. 239-249.
5. Koornneef, J., M. Junginger, and A. Faaij, *Development of fluidized bed combustion—An overview of trends, performance and cost.* Progress in Energy and Combustion Science, 2007. **33**(1): p. 19-55.
6. Gómez-Barea, A. and B. Leckner, *Modeling of biomass gasification in fluidized bed.* Progress in Energy and Combustion Science, 2010. **36**(4): p. 444-509.
7. Winaya, I.N.S., T. Shimizu, and D. Yamada, *A new method to evaluate horizontal solid dispersion in a bubbling fluidized bed.* Powder Technology, 2007. **178**(3): p. 173-178.
8. Pallàres, D., P.A. Díez, and F. Johnsson, *Experimental Analysis of Fuel Mixing Patterns in a Fluidized Bed*, in *The 12th International Conference on Fluidization - New Horizons in Fluidization Engineering*. 2007.
9. Larsson, A., et al., *Using Ilmenite To Reduce the Tar Yield in a Dual Fluidized Bed Gasification System.* Energy & Fuels, 2014. **28**(4): p. 2632-2644.
10. Liu, D. and X. Chen, *Lateral solids dispersion coefficient in large-scale fluidized beds.* Combustion and Flame, 2010. **157**(11): p. 2116-2124.
11. Lim, K.S. and P.K. Agarwal, *Circulatory motion of a large and lighter sphere in a bubbling fluidized bed of smaller and heavier particles.* Chemical Engineering Science, 1994. **49**(3): p. 421-424.
12. Kunii, D. and O. Levenspiel, *Chapter 9: Solid Movement: Mixing, Segregation, and Staging*, in *Fluidization Engineering* 1991.
13. Larsson, A., et al., *Evaluation of Performance of Industrial-Scale Dual Fluidized Bed Gasifiers Using the Chalmers 2–4-MWth Gasifier.* Energy & Fuels, 2013. **27**(11): p. 6665-6680.
14. Leckner, B., et al., *Boundary layers - First measurements in the 12 MW CFB research plant at Chalmers University*, in *11th International Conference on Fluidized Bed Combustion*, E.J. Anthony, Editor. 1991: Montreal p. 771-776.
15. Glicksman, L.R., M.R. Hyre, and P.A. Farrell, *Dynamic similarity in fluidization.* International Journal of Multiphase Flow, 1994. **20**(SUPPL. 1): p. 331-386.
16. Sette, E., D. Pallarès, and F. Johnsson, *Experimental quantification of lateral mixing of fuels in fluid-dynamically down-scaled bubbling fluidized beds.* Applied Energy, 2014. **136**(0): p. 671-681.
17. Kunii, D. and O. Levenspiel, *Chapter 5: Bubbles in Dense Bed*, in *Fluidization Engineering* 1991.
18. NNFCC, *Review of Technologies for Gasification of Biomass and Wastes*. 2009.
19. Hofbauer, H., et al., *Biomass CHP Plant Güssing – A Success Story*, in *Expert Meeting on Pyrolysis and Gasification of Biomass and Waste*. 2002: Strasbourg.
20. Rowe, P.N., et al., *The mechanisms of solids mixing in fluidised beds* Chemical Engineering Research and Design, 1965. **43a**: p. 271-286.
21. Eames, I. and M.A. Gilbertson, *Mixing and drift in gas-fluidised beds.* Powder Technology, 2005. **154**(2–3): p. 185-193.
22. Rowe, P.N. and B.A. Partridge, *An x-ray study of bubbles in fluidised beds.* Chemical Engineering Research and Design, 1997. **75, Supplement**(0): p. S116-S134.
23. Kunii, D. and O. Levenspiel, *Chapter 6: Bubbling Fluidized Beds* in *Fluidization Engineering* 1991.

24. Olsson, J., D. Pallarès, and F. Johnsson, *Lateral fuel dispersion in a large-scale bubbling fluidized bed.* Chemical Engineering Science, 2012. **74**(0): p. 148-159.
25. Niklasson, F., et al., *Estimation of Solids Mixing in a Fluidized-Bed Combustor.* Industrial & Engineering Chemistry Research, 2002. **41**(18): p. 4663-4673.
26. Nixon, M.S. and A.S. Aguado, *Chapter 3 - Basic image processing operations*, in *Feature Extraction & Image Processing for Computer Vision (Third edition)*, M.S.N.S. Aguado, Editor. 2012, Academic Press: Oxford. p. 83-136.
27. Bradski, G. and A. Kaehler, *Learning OpenCV: Computer Vision in C++ with the OpenCV Library*. 2013: O'Reilly Media, Inc. 575.
28. Mohs, G., et al., *Magnetic monitoring of a single particle in a prismatic spouted bed.* Chemical Engineering Science, 2009. **64**(23): p. 4811-4825.
29. Baibich, M.N., et al., *Giant Magnetoresistance of (001)Fe/(001)Cr Magnetic Superlattices.* Physical Review Letters, 1988. **61**(21): p. 2472-2475.
30. Holman, P., *Magnetoresistance (MR) Transducers And How to Use Them as Sensors*. 1 ed. 2004: Honeywell International Inc.
31. Neuwirth, J., et al., *CFD–DEM study and direct measurement of the granular flow in a rotor granulator.* Chemical Engineering Science, 2013. **86**(0): p. 151-163.
32. Wang, X., M.Q. Meng, and C. Hu, *A localization method using 3-axis magnetoresistive sensors for tracking of capsule endoscope.* Conf Proc IEEE Eng Med Biol Soc, 2006. **1**: p. 2522-5.
33. Kunii, D. and O. Levenspiel, *Chapter 4: The Dense Bed: Distributors, Gas Jets, and Pumping Power*, in *Fluidization Engineering* 1991.

8 List of Figures

Figure 1.1	Average annual increases in renewables-based capacity* by regions.	1
Figure 2.1	Schematic of gasifier	4
Figure 2.2	Schematic of the Chalmers Dual Fluidized bed combustor and gasifier	4
Figure 2.3	a) Bubbles rising in a fluidized bed with the velocity ub. b) An erupting bubble on the bed surface results in carryover of particles. c) Schematic of a rising bubble with indication of solids moving around the bubble. [23]	5
Figure 2.4	a) Assumed mixing pattern as exemplified by Olsson et al. [24] based on the results from Pallarès et al. [8]. b) Mechanisms contributing to lateral mixing: bubble eruption scattering (A) and drift sinking (B).	5
Figure 2.5	Gaussian function [26]. (a) Well-known shape of the Gaussian bell. (b) Example of a template for a 5×5 Gaussian filter function.	6
Figure 2.6	Finding optimal value for thresholding [26].	7
Figure 2.7	Effect of camera imperfections on image. (a) Spherical lens bents points away from the optical centre. (b) Miss-alignment of lens and imager causes tangential distortion.	7
Figure 3.1	Schematic of the Chalmers gasifier with installed hot camera probe (side view)	9
Figure 3.2	Schematic of the camera view on the bed	9
Figure 3.3	Schematic of the bubbling fluidized bed used for cold model measurements (side view)	10
Figure 3.4	Photo of the bubbling fluidized bed used for cold model measurements (without bed material)	10
Figure 3.5	Pressure drop over the distributor plate for varying inlet gas velocity and four different distributor plates	12
Figure 4.1	Visualisation of the Laplacian of Gaussian filter in Matlab	13
Figure 4.2	Progress of an image of the camera measurements. (a) Original image of the gasifier. (b) Image after applying LoG function. (c) Histogram of the image after applying LoG function. (d) Image after applying thresholding.	14

Figure 4.3 Calculation of lateral dispersion coefficient from a single particle in a bed with 6 mixing cells by Sette et al. [16] 14
Figure 4.4 Bed expansion according to Monto Carlo method. 17
Figure 5.1 Dispersion coefficient with increasing excess gas velocity 19
Figure 5.2 Height distribution (PDF) of two measurements sampled at 20 Hz and 100 Hz respectively, with the 7x7 1.4 plate at a bed height of 5 cm and a gas inlet velocity of 0.1 m/s. H0 = dense bed height. 20
Figure 5.3 Velocity distribution (PDF) of two measurements sampled at 20 Hz and 100 Hz respectively, with the 7x7 1.4 plate at a bed height of 5 cm and a gas inlet velocity of 0.1 m/s. 21
Figure 5.4 Height distribution (PDF) of measurement sampled at 20 Hz for around 60 min with the 7x7 1.4 plate at a bed height of 5 cm and a gas inlet velocity of 0.1 m/s. 21
Figure 5.5 Height distribution (PDF) of measurement sampled at 20 Hz for around 60 min with the 7x7 1.4 plate at a bed height of 5 cm and a gas inlet velocity of 0.1 m/s after removing trapped particles. 21
Figure 5.6 Particle distribution of measurement sampled at 20 Hz for around 60 min with the 7x7 1.4 plate at a bed height of 5 cm and a gas inlet velocity of 0.1 m/s. 22
Figure 5.7 Particle distribution of measurement sampled at 20 Hz for around 60 min with the 7x7 1.4 plate at a bed height of 5 cm and a gas inlet velocity of 0.1 m/s after removing trapped particles. 22
Figure 5.8 Flow structure of the slice 0.09-0.1 m in x-direction, measured with the 9x9 1.1 plate at a bed height of 3 cm and a gas inlet velocity of 0.13 m/s. Colour bar indicates magnitude of z-direction of the velocity. 23
Figure 5.9 Flow structures of different slices measured at a bed height of 5 cm and a gas inlet velocity of 0.13 m/s. Colour bar indicates magnitude of z-direction of the velocity. (a) 5x5 1.5, slice 0.09-0.1 m in x, (b) 9x9 1.1, slice 0.1-0.11 m in y (c) 7x7 1.4, slice 0.11-0.12 m in y, (d) 5x5 2.6, slice 0.06-0.07 m in y. 23
Figure 5.10 Flow structures of different slices measured with the 5x5 2.6 plate at a bed height of 7 cm. Colour bar indicates magnitude of z-direction of the velocity. (a) 0.07 m/s, slice 0.1-0.11 m in y, (b) 0.13 m/s, slice 0.11-0.12 m in y, (c) 0.2 m/s, slice 0.11-0.12 m in y 25
Figure 5.11 Up-scaled (hot) lateral dispersion coefficient for increasing excess gas velocity. (A) Dy with 5×5 2.6 distributor for bed height of 0.35 and 0.25 m. (B) Dx for 7×7 1.4 distributor for bed height of 0.35 and 0.25 m. (C) Bed height of 0.35 m comparing 5×5 2.6 and 7×7 1.4 distributor plates. 26
Figure 5.12 Lateral dispersion coefficient from literature by courtesy of Sette et al. 27

9 List of Tables

Table 3.1 Measured velocities in Chalmers gasifier (no circulation) 9
Table 3.2 Constant parameters for conditions in the gasifier during measurements 9
Table 3.3 Parameters for hot and cold model 11
Table 3.4 Pressure ratio at different gas velocity for different distributor design 11
Table 5.1 Overview of up-scaled (hot) values for the lateral dispersion coefficient 26

A Appendix A

Robustness

As discussed before the peak of the original 20 Hz measurement for 1 h was reduced to approximately the height of the 100 Hz measurement by removing trapped particles.

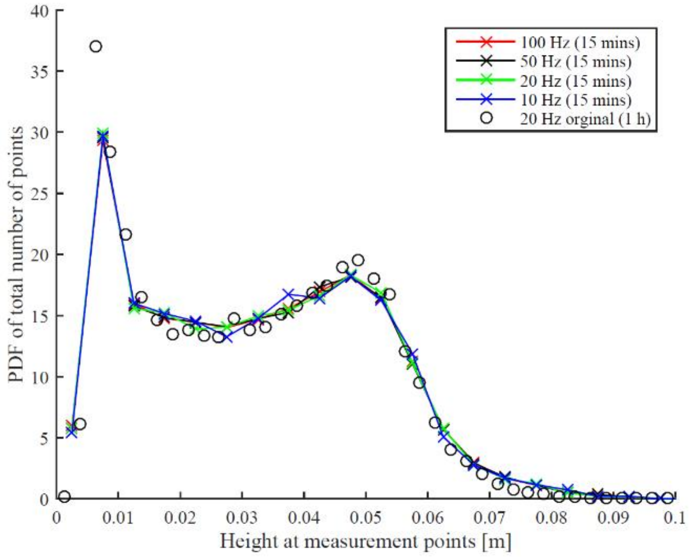

A.1: Height distribution (PDF) of two measurements sampled at 20 Hz and 100 Hz respectively, with the 7x7 1.4 plate at a bed height of 5 cm and a gas inlet velocity of 0.1 m/s. Trapped particles are removed.

The peak of the original 20 Hz measurement for 1 h was moved to the right to similar velocities of the 20 Hz curve of the 100 Hz measurement by removing trapped particles.

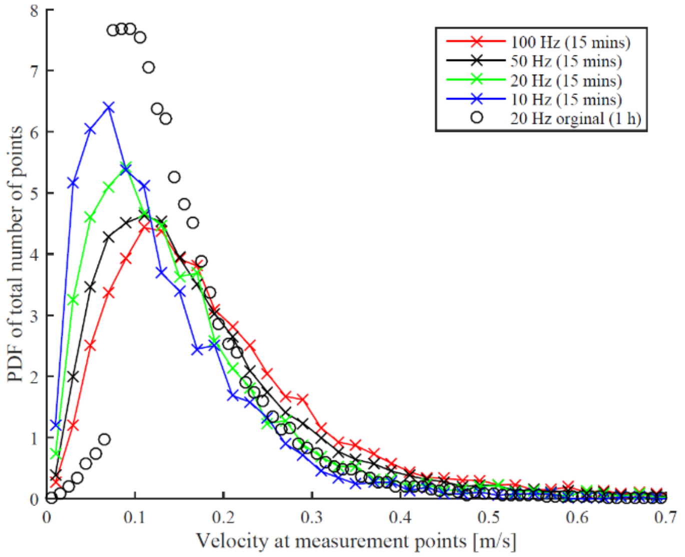

A.2: Velocity distribution (PDF) of two measurements sampled at 20 Hz and 100 Hz respectively, with the 7x7 1.4 plate at a bed height of 5 cm and a gas inlet velocity of 0.1 m/s. Trapped particles are removed.

Pressure drop over the bed

The pressure over the fluidized bed is measured from port 2 to 4. Port 4 is depending on the solid bed height within the solid bed or not which therefore influences the pressure measurements. However, pressure drops from different distributor plates remain comparable as the relative height stays the same.

No pressure drop measurement in the “classical sense”, but pressure drop between the ports. Pressure drop is also independent of inlet gas velocity and therefore set to “constant” for each solid bed height, calculated as mean value for pressure measurements of different gas velocity and then compared between the distributor plates. An increase in the pressure for higher velocity can be assumed to be measurement error as due to higher movement of the bed the port can be filled with bed material and therefore increase the pressure. Erupting bubbles at the ports are assumed to have the same effect.

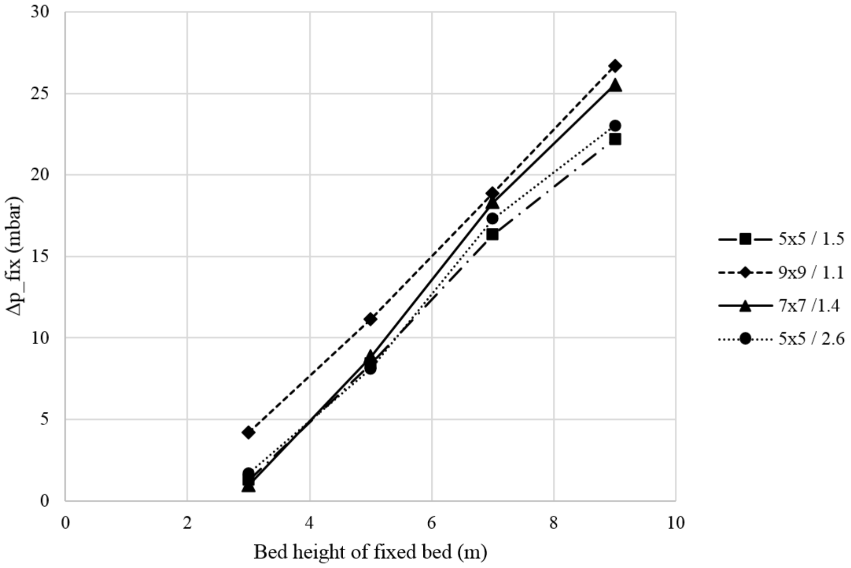

A.3: Pressure drop measured between 2.5 cm and 8.5 cm for increasing fixed bed height.